Assessment of behavioural modification techniques on particle-laden turbulent pipe flows

B. Wolde, L.F. Mortimer & M. Fairweather
School of Chemical & Process Engineering,
University of Leeds, Leeds LS2 9JT, United Kingdom

ABSTRACT

In this study, particle-laden turbulent pipe flows are predicted using direct numerical simulation of the fluid flow in combination with Lagrangian particle tracking and a deterministic energy-based particle agglomeration model, with a particular focus on predicting and elucidating the dynamics of particle-particle interactions. The models used, which were developed and validated in the present work, enhance our understanding of these flows, particularly in regards to the processes which lead to particle collision and agglomeration. The energy-based agglomeration technique is used together with four-way coupling between the particles and the fluid flow to predict particle aggregation due to collision interactions within the flow. Additionally, the impact of behavioural modification techniques, which influence particle dispersion, agglomeration and ultimately particle deposition, is investigated by varying influential parameters such as the temperature and Reynolds number of the flow, and the reduced surface potential, inverse Debye length, Hamaker constant and coefficient of restitution which govern particle-particle interactions. It is concluded that electric double layer repulsion exerts little influence on collision and agglomeration behaviour, attributable to the particle diameters examined being higher in comparison to the effective range of these forces. The study further demonstrates that the restitution coefficient has a significant influence on the behaviour of particle agglomeration, with a decrease in the coefficient resulting in increased aggregation rates. Hamaker constant and Reynolds number variations also both lead to major impacts on particle-particle interaction, with collision and agglomeration events occurring more frequently for increased Hamaker constant and Reynolds number.

Keywords: Turbulent particle-laden pipe flows; Particle collision and agglomeration; DLVO theory; Behavioural modification

1. INTRODUCTION

Particle-laden flows characterised by particles with high density relative to the fluid and complex physical and electrochemical interactions play a crucial role in numerous natural and industrial contexts. Examples include mineral processing (Yang et al., 2019), weather pattern prediction (Geurts et al., 2007), and the spreading of airborne viruses (De-Leon and Pederiva, 2020). Of relevance in this study, the nuclear industry depends on a detailed understanding of particulate flow characteristics in waste suspension systems (Chun et al., 2011). For example, many challenges manifest in transporting historical nuclear waste materials from storage ponds and silos to temporary storage sites. The generation of knowledge regarding particle interaction, collision and aggregation dynamics in these environments is becoming increasingly crucial in developing effective process system designs and ensuring process safety. Predicting the long-term morphology of particles (including size, shape and their interaction dynamics) over extended flow durations is also essential in anticipating potential processing complications and challenges in current and future waste transport system designs.

These applications demonstrate the significance of comprehending both particle-level and bulk scale dynamics in predicting a flow's long-term emergent behaviour. Despite being significant in many industrial processes, however, very few studies based on direct numerical simulation (DNS) have been performed in the past to investigate turbulent pipe flows in the presence of a particulate phase. In those limited cases, multiphase DNS investigations have mainly used one-way coupling between the particles and the fluid flow, and the simulations have generally been at low Reynolds numbers (Rani et al., 2004; Picano et al., 2009; Kuerten, 2016). There is a noticeable absence of four-way coupling and particle agglomeration studies, particularly in cylindrical geometries, despite most industrial flows possessing high volume fractions where interactions between particles are of importance to phenomena such as preferential concentration and deposition. Analysing one-way coupled flows does, however, provide insight into the underlying physical mechanisms governing the interaction between the fluid flow and particle trajectories, with the understanding generated being crucial for predicting and controlling behaviours in practical applications.

Previous investigations conducted under dilute flow conditions have significantly contributed to identifying and comprehending key dispersive characteristics of turbulent flows

laden with particles. One-way coupled simulations reveal that two primary mechanisms drive particle migration and localised concentration increases: preferential accumulation and turbophoresis. Computational analyses (Elghobashi and Truesdell, 2006; Squires and Eaton, 1991; Eaton and Fessler, 1994) suggest that preferential accumulation is most prominent around particle Stokes numbers of order unity, where the Stokes number is based on the Kolmogorov timescale. In this regime, particles tend to aggregate in regions characterised by low velocity magnitudes, a phenomenon also validated experimentally (Fessler et al., 1994). Turbophoresis describes a particle's tendency to migrate towards regions of low turbulence kinetic energy, a behaviour observed to scale initially with the Stokes number, though saturate at increased values (Kuerten and Vreman, 2005; Marchioli et al., 2008; Marchioli and Soldati, 2002; Zahtila et al., 2023). Small amounts of surface roughness can dramatically reduce wall accumulation effects by disrupting turbophoresis as shown in Chan et al. (2021). Furthermore, wall-resolved LES studies have shown that particle-particle collisions play a crucial role in shaping wall-normal concentration profiles (Johnson et al., 2020). As particles approach wall regions, they interact with local turbulence structures, exhibiting a diverse range of behaviours contingent upon their inertial properties (Mortimer et al., 2019). Fairweather and Yao (2009) investigated particle dispersion in a turbulent duct flow at a bulk Reynolds number of 250,000, considering a wide range of particle sizes from 5 to 1000 μm (equivalent to $St^+ = 0.24$ to 9661) using coupled large eddy simulation (LES) and Lagrangian particle tracking (LPT). Gravity was shown to have the greatest influence on larger particles, causing deposition, while the secondary flows in the plane of the duct cross-section were determined to be the major factor responsible for smaller particle dispersion. Particle resuspension, or the migration of particles from the duct wall to the bulk flow, was also examined by Yao and Fairweather (2010) using similar techniques to those employed by Fairweather and Yao (2009). Particle sizes ranged from 5 to 500 μm, with force contributions from lift, drag, buoyancy and gravity taken into account when analysing the motion of the particles. This work again demonstrated that secondary flows have a significant effect on particle resuspension.

With advances in computational power it has now become possible to perform more complex particle-laden flow simulations considering a wider range of phenomena which are important in predicting the long-term dispersive and aggregation behaviour of industrial flows. Vreman et al. (2009) used LES to investigate the effect of four-way coupling in a vertical turbulent multiphase channel flow, concluding that particle collisions must be taken into account in order to accurately

simulate particle phases with volume fractions of approximately $\phi_P \sim 10^{-2}$, affirming Elghobashi's (2007) previous findings. Breuer et al. (2012) carried out a four-way coupled LES-LPT of a turbulent channel flow using a bulk Reynolds number, $Re_B = 11{,}900$, with these authors providing an effective deterministic search technique that lowers the computational complexity from $O(N_P^2)$ to $O(N_P)$ in determining interparticle collisions (for number of particles N_P).

Research focusing on post-collision phenomena such as particle agglomeration in turbulent flows is limited, despite the prevalence of electrokinetic interaction dynamics in most real liquid-solid flow systems. Typically, particles either rebound off one another or adhere, forming aggregates (Henry et al., 2013). Schutte et al. (2015) investigated the impact of a 'hit and stick' agglomeration model on particle aggregation, breakup, deposition and re-entrainment in turbulent channel flows. They observed comparable behaviour between results based on large eddy simulation and direct numerical simulation and noted that two-way coupling influenced the characteristics of the agglomerates. In order to predict collisions and agglomeration in an LES of a turbulent channel flow, Njobuenwu and Fairweather (2017) employed a deterministic approach based on techniques developed by Breuer and Almohammed (2015). These authors incorporated the van der Waals force and an energy-balance based agglomeration condition, conducting parametric simulations on the effect of the restitution coefficient, $e_n = 0.2$ to 0.8, particle size, $d_p = 60$ to 316 μm, shear Reynolds number, $Re_\tau = 150$ to 590, and particle concentration, $\phi_p = 5 \times 10^{-4}$ to 5×10^{-3}, on the resulting agglomeration behaviour. An increase in aggregation rate with decreasing restitution coefficient was identified, and collisions were more frequent for smaller particles as well as such particles being most efficient in forming agglomerates. Particle-particle interactions also showed a strong dependency on the flow Reynolds number, and increases in particle concentration were also shown to enhance agglomeration. Mortimer et al. (2020) extended the use of Njobuenwu and Fairweather's (2015) deterministic model using DNS, investigating particle agglomeration in a fully coupled turbulent channel flow simulation at shear Reynolds number, $Re_\tau = 180$. They also studied the effect of particle size, $d_p = 202$, 286 and 405 μm at a fixed volume fraction, $\phi_P = 10^{-3}$. Their findings demonstrated that collision rates rise with particle size at a constant particle concentration but remain similar for all particle sizes at a set volume fraction. They also observed that smaller particles tend to agglomerate faster to form larger clusters, and that increased collision occurrences were observed close to the walls,

though agglomeration was more likely to take place in the bulk of the channel due to lower collision kinetic energies.

The model developed by Njobuenwu and Fairweather (2015), extended by Mortimer et al. (2020), is used in the present work, with the model adapted accordingly for the pipe geometry under consideration, and with full DLVO theory (Derjaguin and Landau, 1941; Verwey and Overbeek, 1955) terms incorporated to predict particle interactions. By using high-accuracy and robust simulation approaches, the impact of behavioural modification techniques on particle dispersion and agglomeration is investigated using fully coupled DNS-LPT. Behavioural modification techniques are considered to study how modifying key parameters of interest can be used to obtain a desired flow property. A fully resolved particle-laden turbulent pipe flow with shear Reynolds number $Re_\tau = 360$ based on pipe radius R, is used to simulate four-way coupled flows with agglomeration at high particle concentrations with a volume fraction, $\phi_P \geq 10^{-3}$ (except when studying the influence of flow Reynolds number when a Re_τ = 180 flow is also considered). Such a high concentration is required to encourage particle collisions and ensure sufficient agglomeration of particles (Ferrante and Elghobashi, 2003; Njobuenwu and Fairweather, 2017). The variation of important parameters in DLVO theory is investigated to determine the impact of behavioural modification effects which change the kinematics of the particle collisions. The reduced surface potential ($\Theta =$ 16, 20 and 24 mV), inverse Debye length, ($\kappa =$ 3.04 $\times$ 10^{-9}, 3.04 $\times$ 10^{-8} and 3.04 $\times$ 10^{-10} m), ambient temperature of the suspension (T_f =264, 293 and 322 K), coefficient of normal restitution ($e_n =$ 0.2, 0.4 and 0.6), Hamaker constant ($H =$ 7.84, 22.3 and 36.76 zJ) and shear Reynolds number ($Re_\tau =$ 180 and 360) of the flow are all examined. According to the work of Mortimer and Fairweather (2021), these variables, particularly those associated with the van der Waals interaction (Hamaker constant) and collision kinematics (coefficient of restitution), have been found to have the greatest influence on collision dynamics in particle-laden channel flow simulations and are therefore further studied in the current pipe geometry.

2. METHODOLOGY

2.1 Single-phase flow

To solve the Navier-Stokes equations as a DNS, computational fluid dynamic solver, Nek5000 (Fischer, 2008) has been used. This solver is based on the spectral element method and employs a high-order weighted residual technique. Nek5000 is favourable here due to its high accuracy and low numerical dispersion and dissipation, and is easily and efficiently parallelisable. It has been used widely throughout the DNS literature for both single-phase and particle-laden flows in recent decades (El Khoury et al., 2013; Mortimer et al., 2020).

Nek5000 solves the Navier-Stokes equations in non-dimensional form. Below, the non-dimensional variables are defined which are used to obtain the non-dimensional version of the Navier-Stokes equations in Nek5000:

$$\boldsymbol{x}^* = \frac{\boldsymbol{x}}{D},\ \boldsymbol{u}^* = \frac{\boldsymbol{u}}{U_B}\ ,\ t^* = \frac{t}{D/U_B}\ ,\ \ p^* = \frac{p}{\rho {U_B}^2}. \tag{1}$$

Using the above, the Navier-Stokes equations can be non-dimensionalised as follows:

$$\nabla \cdot \boldsymbol{u}^* = 0, \tag{2}$$

$$\frac{\partial \boldsymbol{u}^*}{\partial t^*} + (\boldsymbol{u}^* \cdot \nabla)\boldsymbol{u}^* = -\nabla p^* + \frac{1}{Re_B}\nabla \cdot \boldsymbol{\tau}^* + \boldsymbol{f}_i^*. \tag{3}$$

Here, $\boldsymbol{u}^*(\boldsymbol{x}^*, t^*)$ is the fluid velocity vector, non-dimensionalised using the bulk velocity, U_B. The position vector, $\boldsymbol{x}^*$, and time, t^*, are non-dimensionalised as $x^* = \frac{x}{D}$ and $t^* = \frac{t}{D/U_B}$, respectively, with D the pipe diameter. The term p^* is the non-dimensionalised pressure for high-velocity flows, with $p^* = \frac{p}{\rho {U_B}^2}$, and ρ the fluid density. The bulk Reynolds number Re_B based on pipe diameter is already non-dimensional and defined as $Re_B = U_B D/\nu$, with ν the kinematic viscosity of the fluid phase. Note that bulk Reynolds numbers quoted hereon assume that the pipe diameter is the bulk length scale due to the formulation used in Nek5000, and in line with previous studied (Boersma, 2013; Eggels et al., 1994). As such, the subscript D in the Reynolds number will be omitted from here on. Finally, $\boldsymbol{\tau}^*$ is the non-dimensionalised stress tensor, $\boldsymbol{\tau}^* = \nabla \boldsymbol{u}^* +$

$\nabla \boldsymbol{u}^{*T}$, and $\boldsymbol{f}_i^*$ is a generic body forcing term, in the context of pipe flows representing both the driving pressure gradient and the two-way interaction between the fluid and the particles, detailed later.

Eqs. (2) and (3) are solved numerically using the spectral element method along with appropriate boundary conditions. In three-dimensional space, these equations are discretised as grid points by the Lagrange-Galerkin approximation method. N^{th}-order Lagrange polynomial interpolants on Gauss-Lobatto-Legendre (GLL) points are implemented as a basis for velocity space, and Lagrangian interpolants of order N-2 on Gauss-Legendre quadrature points are employed for pressure space.

2.2 Particle equations of motion and two-way coupling

The particle equations of motion for all forces considered in the flows encountered in this study are described below, based on a modified Maxey and Riley (1983) equation. The particle equations motion in the turbulent flow are obtained by solving Newton's second law of motion for each spherical particle. Equation (4) represents the sum of all the forces applied in the force-balance equation:

$$\sum \boldsymbol{F}_N = \boldsymbol{F}_D + \boldsymbol{F}_L + \boldsymbol{F}_V + \boldsymbol{F}_P + \boldsymbol{F}_A. \tag{4}$$

Here, $\boldsymbol{F}_N$ is the sum of all the hydrodynamic and body forces acting on each particle. $\boldsymbol{F}_D$ is the drag force, $\boldsymbol{F}_L$ the lift force, $\boldsymbol{F}_V$ the virtual added mass force, $\boldsymbol{F}_p$ the pressure gradient force and $\boldsymbol{F}_A$ represents any additional body forces present, such as gravity. In Nek5000, equations are solved in non-dimensional form. As such, each component of the particle equation needs to be transformed, such that the solver deals with solely non-dimensional variables for both the fluid and particle phases. The particle Stokes numbers, representing the ratio of the particle time scale to a particular fluid timescale, based on the bulk and shear timescales, are given by Eqs. (5) and (6), respectively:

$$St_B = \frac{\tau_p}{\tau_{f,B}} = Re_B \frac{\rho_p^* {d_p^*}^2}{18 f_D}, \tag{5}$$

$$St_\tau = \frac{\tau_p}{\tau_{f,\tau}} = Re_\tau^2 \frac{\rho_p^* {d_p^*}^2}{18 f_D}. \tag{6}$$

Here, τ_P is the particle timescale, $\tau_{f,B}$ and $\tau_{f,\tau}$ are the bulk and shear fluid timescales, respectively, $\rho_p^* = \rho_P/\rho$ is the density ratio, $d_P^* = d_P/D$ is the non-dimensional particle diameter, and f_D is the non-dimensional Stokes drag function taken from Schiller (1934) and Clift et al. (2005). Using Eqs. (5) and (6), one can then obtain the following expression:

$$\frac{St_\tau}{St_B} = \frac{Re_\tau^2}{Re_B}. \tag{7}$$

The LPT solves a force-balance equation for each particle in the system, represented as an impenetrable computational sphere under the assumption of point particles. The particle equations of motion for all forces considered are presented in Eqs. (8) and (9), such that the non-dimensional form of the equations for spherical particles, as implemented in the simulations, is:

$$\boldsymbol{u}_p^* = \frac{\partial \boldsymbol{x}_p^*}{\partial t^*}, \tag{8}$$

$$\frac{\partial \boldsymbol{u}_P^*}{\partial t^*} = \frac{1}{M_{VM}} \left[\underbrace{\frac{3 C_D |\boldsymbol{u}_s^*|}{4 d_p^* \rho_P^*} \boldsymbol{u}_s^*}_{Drag} + \underbrace{\frac{3}{4} \frac{C_L}{\rho_P^*} (\boldsymbol{u}_s^* \times \boldsymbol{\omega}_F^*)}_{Lift} + \underbrace{\frac{1}{2\rho_P^*} \frac{D' \boldsymbol{u}_F^*}{Dt^*}}_{Virtual\ Mass} + \underbrace{\frac{1}{\rho_P^*} \frac{D \boldsymbol{u}_F^*}{Dt^*}}_{Pressure\ Gradient} + \underbrace{\frac{1}{Fr}\left(1 - \frac{1}{\rho_p^*}\right) \widehat{\boldsymbol{g}^*}}_{\text{Gravity}} \right]. \tag{9}$$

In Eqs. (8) and (9), $\boldsymbol{u}_p^*$ is the non-dimensional particle velocity vector, $\boldsymbol{x}_p^*$ the non-dimensional particle position vector, C_D the drag coefficient, and $\boldsymbol{u}_s^*$ the slip velocity given as $\boldsymbol{u}^* - \boldsymbol{u}_p^*$. The term $\boldsymbol{\omega}_F^*$ represents the vorticity of fluid, which is given by $\boldsymbol{\omega}_F^* = \nabla \times \boldsymbol{u}^*$, and the full equation is divided by $M_{VM} = (1 + 1/2\, \rho_p^*)$ to account for the virtual mass force. The drag force occurs due to particle movement through a resistive fluid phase and is the dominant force in fluid-particle flows (Schiller and Naumann, 1935), while the lift force arises due to shear across the particle. Saffman (1965) studied the strength and direction of the lift force for low particle Reynolds

numbers and later Dandy and Dwyer (1990) extended this work to high particle Reynolds numbers. The virtual mass and pressure gradient forces were based on the fluid acceleration and local pressure gradient, respectively (Stokes, 1851). The term, Fr is the Froude number, defined as $\mathrm{F}r = U_B^2/gD$, with g the gravitational acceleration and $\widehat{\underline{g^*}}$ a unit vector in the direction of gravitational attraction.

For two-way coupling, the additional momentum source term in the Navier-Stokes equations, $\boldsymbol{f}_i^*$, includes solely the drag force acting on the particles, in line with previous work, (Zhao et al., 2010; Lee and Lee, 2015), as well as previous studies demonstrating its dominance in terms of magnitude relative to other hydrodynamic contributions such as lift and added mass (Mortimer et al., 2019). The term is computed as: $\boldsymbol{f}_i^* = \sum_j^{N_{P,i}} \boldsymbol{a}_{P,j}^* / V_i^*$, with $\boldsymbol{a}_{P,j}^*$ the acceleration contributions from the drag force on the particle, V_i^* the volume of the computational cell and j an index which iterates over the number of particles contained within the corresponding cell, $N_{P,i}$. This technique has been validated in our previous work (Mortimer et al., 2020). In the present implementation of two-way coupling, only the drag force contribution from the dispersed phase is included in the feedback to the carrier phase. Lift and virtual mass forces are applied to the particle motion but are omitted from the feedback to the fluid. This approach follows previous work (e.g., Zhao et al., 2010; Lee and Lee, 2015; Mortimer et al., 2019), where drag was shown to dominate the overall momentum exchange. Nevertheless, this simplification introduces a limitation due to the lower density-ratio considered in this study, as the neglected terms may become locally significant in regions of strong velocity gradients, particularly near the wall, where shear-induced lift and pressure forces can alter turbulence structure and particle dispersion. The effect of these forces on local turbulence modulation is therefore not captured in the present simulations.

2.3 DLVO interaction forces and agglomeration

The dynamics involved in resolving inter-particle collisions was further extended to include the potential agglomeration of colliding particles. A deterministic hard sphere collision model, as implemented in Breuer and Almohammed (2015) and Njobuenwu and Fairweather (2017), was used to predict particle agglomeration. In this model, particles and their agglomerates are modelled as constituent equivalent-volume point spheres. Particle agglomeration is assumed to occur if the total kinetic energy of the collision is insufficient to overcome the attractive van der Waals

potential of the DLVO force between the two colliding particles, taking into account the energy dispersed upon particle compression as the two particles collide (Derjaguin and Landau, 1941; Verwey and Overbeek, 1955). The equation for the full DLVO attraction and/or repulsion caused by a spherical particle, p_1, on spherical particle p_2, is given by:

$$F_{TOT} = F_{vdW} + F_{EDL}. \tag{10}$$

Here, F_{vdW} is the attractive van der Waals term and F_{EDL} is the electric double layer term in the DLVO equation. The van der Waals attraction is as follows:

$$F_{vdW} = \frac{H}{12h^2} f, \tag{11}$$

where *H* is the Hamaker constant, h the inter-surface distance between spheres, and f is a factor depending on the geometry of the colliding surfaces. For two spheres of diameter, $d_1 \gg \delta$ and $d_2 \gg \delta$ in contact at a small distance $h = \delta$, f is equal to $\frac{2d_1 d_2}{d_1 + d_2}$. The electric double layer repulsion is expressed as:

$$F_{EDL} = \frac{64\pi r_p n k_B T_f \Theta^2 e_c^{-kh}}{k} \hat{n}, \tag{12}$$

with,

$$\Theta = tanh\left(\frac{z e_c \varphi}{4 k_B T_f}\right), \tag{13}$$

and

$$k = \sqrt{\frac{2nz^2 e_c^2}{\varepsilon_0 \varepsilon_r k_B T_f}}. \tag{14}$$

In the above equations, r_p is the particle radius, *n* is the number density of electrolyte ions, k_B is the Boltzmann constant, T_f is the temperature of suspension, Θ is the reduced surface potential,

and κ is the inverse Debye length. Additionally, z is the electrolyte ionic valency, e_c is the elementary electric charge, φ is the zeta potential, ε_0 is permittivity of vacuum, ε_r is the relative permittivity of solvent and $\hat{n}$ is a unit vector on the particles. One can obtain the van der Waals energy between two spheres by integrating Eq. (11) with respect to the distance between the spheres:

$$\Delta E_{vdW} = \frac{HA}{12\pi h}, \tag{15}$$

where A is the contact area. For small deformations, $d_1 \gg h_1$ and $d_2 \gg h_2$, the contact area can be expressed as:

$$A = \pi d_1 h_1 = \pi d_2 h_2, \tag{16}$$

where h_1 and h_2 are the depths of the deformation. The expressions for h_1 and h_2 are determined by the work required to deform a ductile material (Breuer and Almohammed, 2015):

$$h_1 = d_1 d_2^2 |\boldsymbol{u}_2^- - \boldsymbol{u}_1^-| \left[\frac{\rho_1\rho_2(1-e_n^2)}{6\bar{\sigma}(d_1+d_2)(\rho_1 d_1^3 + \rho_2 d_2^3)}\right]^{\frac{1}{2}} \tag{17}$$

Similarly, the electrical double layer caused by the spherical particles can be expressed as:

$$\Delta E_{EDL} = \frac{2\sigma^2}{\varepsilon_0\varepsilon_r k} e^{-kh_1}. \tag{18}$$

The energy-balance based non-dimensional agglomeration condition is given in Eq. (19) where, if the particle-particle resultant collision energy is sufficiently low, then an agglomeration occurs, otherwise the particles recoil using an inelastic hard-sphere calculation:

$$\boldsymbol{u}_{p,r}^{*^2} - \frac{(1-e_n^2)(\boldsymbol{u}_{p,r}^* \cdot \hat{\boldsymbol{n}})^2}{|\boldsymbol{u}_{p,r}^* \cdot \hat{\boldsymbol{n}}|} \leq \frac{H^*}{6\delta_0^{*^2}} \left[\frac{6(1-e_n^2)}{\pi^2 \rho_p^* \bar{\sigma}^*} \left(\frac{d_{p,1}^{*^3} + d_{p,2}^{*^3}}{d_{p,1}^{*^2} d_{p,2}^{*^2} (d_{p,1}^* + d_{p,2}^*)}\right)\right]^{\frac{1}{2}} \tag{19}$$

$$+\frac{2}{\varepsilon_r k^*}\left(\frac{\Theta^2}{\varepsilon_0}\right)^* e^{-k^* {h_1}^*}$$

Here, the superscript * represents dimensionless quantities obtained using bulk flow parameters. Additionally, $\boldsymbol{u}_{p,r}^*$ is the relative particle collision velocity, e_n is the normal coefficient of restitution, $H^* = H/\rho U_B^2 D$ is Hamaker constant, $\delta_0^* = \delta_0/D$ is the minimum contact distance, $\rho_p^* = \rho_p/\rho$ is the particle-fluid density ratio, $\bar{\sigma}^* = \bar{\sigma}/(\rho U_B^2)$ is the yield pressure and $d_{p,1}^*$ and $d_{p,2}^*$ are the first and second colliding particle diameters. Also, $\hat{\boldsymbol{n}}$ is the unit vector, $k^* = kD$ the inverse Debye length, ${h_1}^* = d_{p,1}^* d_{p,2}^{*2}\left|\boldsymbol{u}_{p,r}^*\right|\left[\rho_{p,1}^*\rho_{p,2}^*(1-e_n^2)/6\bar{\sigma}^*(d_{p,1}^*+d_{p,2}^*)(\rho_{p,1}^* d_{p,1}^{*3} + \rho_{p,2}^* d_{p,2}^{*3})\right]^{1/2}$ is the depth of the deformation and $[\Theta^2/\varepsilon_0]^* = \Theta^2/\varepsilon_0\,\rho_f U_B$ is the square of the ratio of the reduced surface potential to the permittivity of free space.

Agglomerates formed are given new diameters based on the volume of a larger sphere equal to that of the sum of the volumes of the constituent colliding particles (Mortimer et al., 2020; Breuer and Almohammed, 2015) if the requirements of Eq. (19) are met. The agglomerate's new velocity, u_{agg}^* and position r_{agg}^* are given by:

$$u_{agg}^* = \frac{1}{{d_{agg}^*}^3}\left({d_{p,1}^*}^3 u_1^* + {d_{p,2}^*}^3 u_2^*\right), \tag{20}$$

where $$d_{agg}^* = \sqrt[3]{{d_{p,1}^*}^3 + {d_{p,2}^*}^3},$$

and $$r_{agg}^* = \frac{1}{2}(r_1^* + r_2^*) + t_{col} u_{agg}^*, \tag{21}$$

where $d_{p,1}^*$ and $d_{p,2}^*$ are the non-dimensional diameters of the first and second colliding particles, u_1^* and u_2^* are the collision velocities, r_1^* and r_2^* are the collider positions and t_{col} is the overlap time during the collision (Mortimer et al., 2019). As agglomeration progresses, some particle structures may increase in size such that their equivalent diameters may approach or exceed the size of the smallest near-wall grid cells. Because all particles and agglomerates are treated using a point-particle assumption, it should be noted that this introduces an additional

uncertainty in predicting near-wall collision and agglomeration behaviour for larger agglomerates, where finite-size and wall-interaction effects can be more pronounced.

2.4 Pipe flow domain

The computational domain, as illustrated in Figure 1 (upper), consisted of a circular pipe of diameter D and characteristic length L=12.5$D \approx 4\pi D$, partitioned into 36,576 spectral elements, equivalent to 18,726,912 GLL grid points. Within each element, the velocity is represented by high-order tensor-product Gauss-Lobatto-Legendre polynomial expansions of order *N*. The shear Reynolds number, based on the shear velocity and pipe diameter, was used to characterise each pipe flow studied. In the present work, $Re_\tau \approx$ 139, 180 and 360 turbulent flows were considered, with equivalent bulk Reynolds numbers 3,975, 5,300 and 11,700, respectively. The minimum and maximum grid resolution in wall units was Δr^+ = (0.14, 4.77), $\Delta(r\theta)^+$= (1.51, 4.93) and Δz^+= (3.03, 7.42), which are similar to those used in previous single-phase studies (El Khoury et al., 2013). The spectral elements method is a high-order weighted residual technique that splits the domain into several hexahedral subdomains, or elements, that comprise the entire system. For all simulations, the same mesh topology and number of spectral elements was used, ensuring sufficient elements such that the Kolmogorov scale conditions required for DNS were met. GLL quadrature points ($N = 7$, which corresponds to 83 grid-points per element) were used to distribute the vertices in each element. Periodic boundary conditions were applied in the streamwise direction, and no-slip conditions at the wall for the radial velocity components.

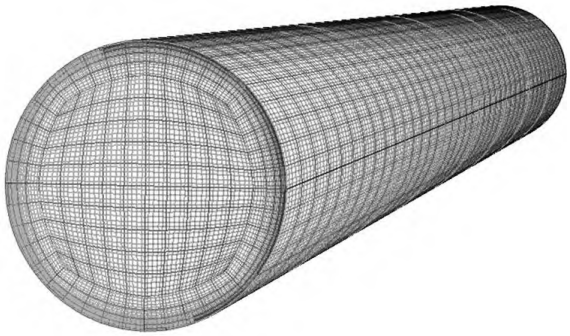

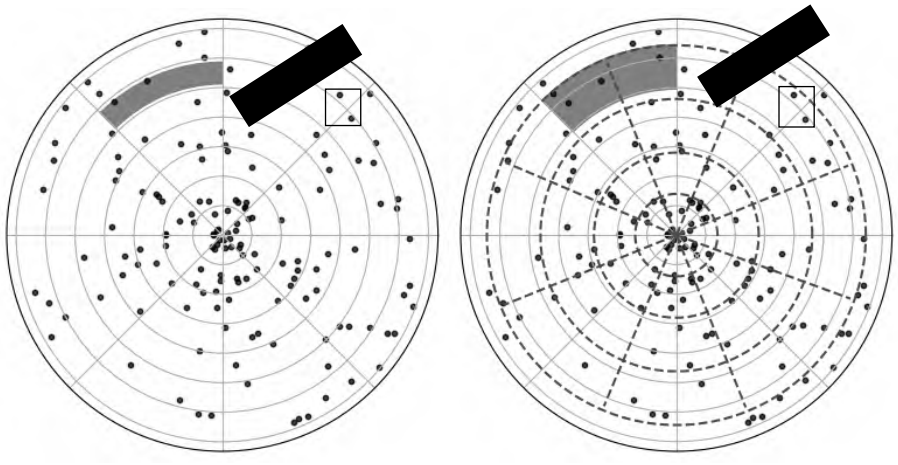

Figure 1: The computational mesh topology with Gauss–Lobatto–Legendre quadrature points (N = 7) for all simulations (upper). Initial (lower-left) and secondary (lower-right) virtual search grids for deterministic binary collision identification (see, also, Breuer et al. (2012) and Mortimer et al. (2020)).

2.5 Hard-sphere collision algorithm and boundary interactions

The simulations were performed four-way coupled, accounting for collisions between particles. A deterministic, hard-sphere, elastic collision model was utilised. A deterministic grid-based binary collision search algorithm was also used to reduce computational cost. As the particles are rigid and undeformable, it is reasonable to assume that the particle collision contact time is shorter than the LPT time-step and this was ensured, such that particle collisions were not missed, by reducing the time step such that the distance travelled by a particle in a single time step was less than the diameter of the particle. By comparing the relative collision velocities of the particles upon impact, the approach can identify which have collided and calculate rebound velocities. Other particle-particle forces acting on the collisions were considered insignificant. To examine hard-sphere elastic collisions more precisely under four-way coupling conditions, a volume fraction, $\phi_P \geq 10^{-3}$, was utilised, as discussed earlier (Mortimer et al. 2020). In Figure 1, the first virtual collision search grid (left) and second coarser virtual search grid (right) are depicted. The particles are divided into user-specified numbers of cells within both search grids at each timestep. Figure 1 (left) serves as an illustration of a missed collision, rectified using the secondary mesh as shown in the right-hand panel. Particle collisions with the pipe wall are treated fully elastically such that in a particular timestep, if a particle exceeds the wall boundary at $r_P > R$, the particle is

reintroduced back into the domain by backtracking its trajectory during that timestep and the velocity vector is reflected against the normal to the wall where the particle first penetrated it. Particles exiting any of the two periodic boundaries in the streamwise direction are reinjected at the appropriate location on the opposite boundary.

3. RESULTS AND DISCUSSION

3.1 Single-phase and multiphase flow validation

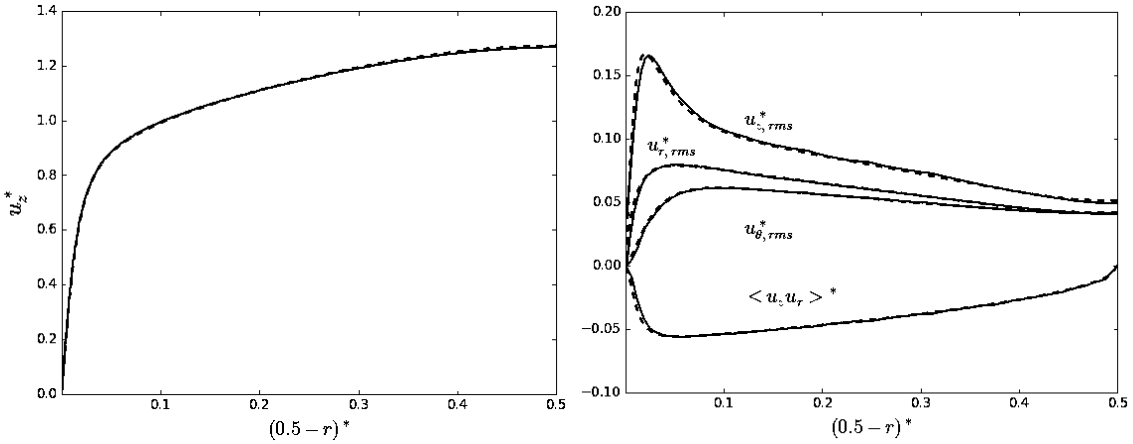

Figure 2: Mean streamwise velocity profiles and rms fluctuating velocity and shear stress profiles at Re_τ = 360. The axial, $u'^*_{z,rms}$, radial, $u'^*_{r,rms}$, azimuthal, $u'^*_{\theta,rms}$ normal stresses and Reynolds shear stress, $< u'_z u'_r >^*$ profiles are compared against DNS datasets. −: present DNS, − −: El Khoury et al. (2013) DNS,

To establish the accuracy of the solver, a single-phase turbulent pipe flow at $Re_\tau = 360$ based on D was first performed and compared against the equivalent DNS results of El Khoury et al. (2013). The mean streamwise velocity and the second-order statistics presented in Figure 1 are shown to be in very close agreement with the reference data across most of the pipe radius. Any small deviations are confined to the immediate near-wall region and lie within typical DNS variability. This level of agreement demonstrates that the present single-phase baseline is robust and suitable for the subsequent multiphase studies. As an additional check, the streamwise kinetic-energy spectrum $E^*(k^*)$ was examined for the same case. The spectrum exhibits a clear inertial subrange with a strong $k^{-5/3}$ trend before rolling off at high wavenumbers, consistent with expectations for fully developed turbulent pipe flow at this Reynolds number.

Simulations for multiphase flow validation purposes were performed at $Re_\tau \approx 180$ and 139, with the findings directly compared with the DNS results of Rani et al. (2004) and Vreman (2007) who also considered particles within the same flow configuration. To initialise the $Re_\tau \approx 180$ simulation, 420,000 particles were randomly injected, and each particle was assigned its surrounding fluid velocity through spectral interpolation. Note that the initial fluid condition was taken from a statistically stationary single-phase turbulent pipe flow performed in advance of the study. Figure 3(a, b) demonstrates the coupled effect of the particles on the continuous phase flow field compared to the results of Rani et al. (2004) at $Re_\tau \approx 180$. Note that these authors do not provide results for the particle phase statistics.

The mean streamwise fluid velocity profile of the present work is compared against the DNS of Rani et al. (2004) at a particle Stokes number based on the shear timescale of $St^+ \cong 58$. The mean streamwise velocities are shown to be in good agreement. This simulation used the highest concentration of particles present in the two validation cases, which had a volume fraction equivalent to $\phi_P = 1.79 \text{ x } 10^{-4}$. Figure 3(b) displays the root mean square of the axial, radial and azimuthal fluctuating fluid velocities, together with the mean Reynolds shear stress $< u_z' u_r' >^*$ at $Re_\tau = 180$. Compared to the DNS of Rani et al. (2004), both sets of results again show good agreement. Although not shown in Figure 3, turbulence attenuation, particularly in the bulk flow region, was also observed on switching from one- to four-way coupling in the present work and was found to be similar in magnitude to that of the comparison study.

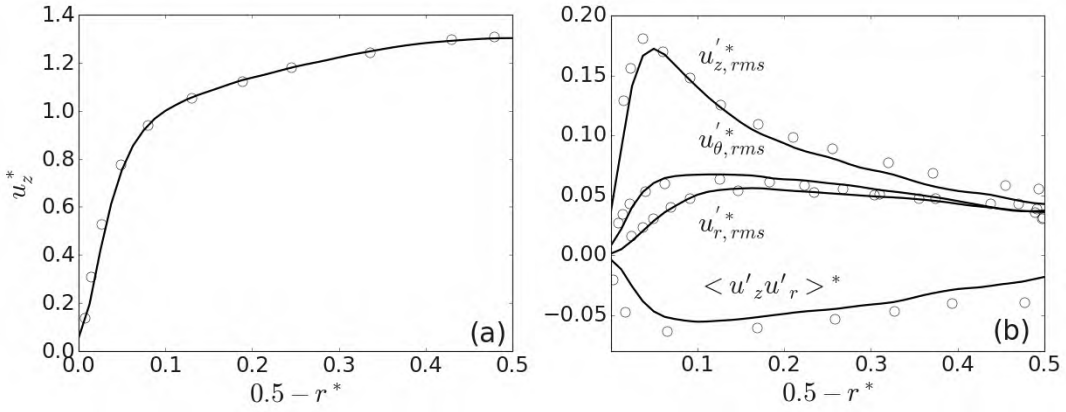

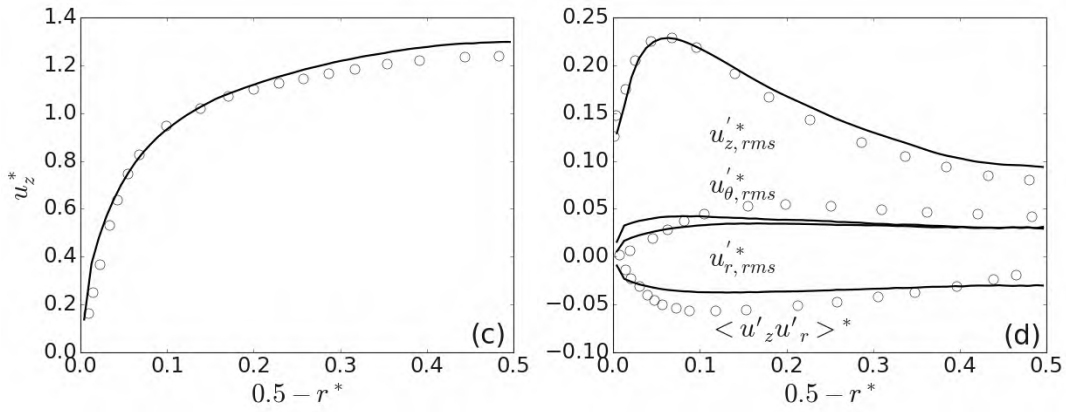

Figure 3: Effect of coupled fluid-particle flow on (a) mean axial fluid velocity and (b) fluid normal and shear stresses at $Re_\tau = 180$, and on (c) mean axial particle velocity and (d) particle normal and shear stresses at $Re_\tau = 139$ (— present DNS four-way coupled; ○ Rani et al. (2004) and Vreman (2007) DNS four-way coupled).

The particulate phase mean streamwise velocity, rms velocity fluctuations and shear stress profiles are compared against the four-way coupled DNS findings of Vreman (2007) at $Re_\tau \approx 139$ based on the pipe diameter in Figure 3(c, d). For validation purposes, gravitational forces were also included in the streamwise direction to replicate the original vertical pipe flow configuration and ensure consistency in comparison. In contrast, for the remaining main liquid-solid agglomeration simulations presented in this study, gravity was deliberately omitted. This decision was made to isolate the effects of turbulence-induced collisions and DLVO interaction forces on particle agglomeration, avoiding the added complexity of buoyancy-driven motion. Consequently, only drag, lift, virtual mass, pressure gradient and interparticle interaction forces were considered in the main simulations. A spherical $60\ \mu m$ particle diameter was chosen in this case with 29,400 particles used in the simulation, matching that of the reference study. Here, the gravitational force was applied in the streamwise direction; hence a vertical pipe was simulated. The only difference was that in the present simulation a much larger number of numerical grid nodes was used (18.7M nodes as opposed to 607k). Statistical data was collected from the fully-coupled simulations after several particle response times ($t^* = 20$), ensuring sufficient time for the injected phase to adapt to the surrounding fluid flow. The particle mean velocity profile and stresses compare reasonably with the results of Vreman (2007). Some differences do occur within the bulk flow region, however, this likely due to the significantly increased numerical resolution used in the present work.

3.2 Influence of electric double layer repulsion

An initial study was undertaken in order to justify use of the energy-based particle agglomeration model by assessing the impact of the electric double layer repulsion term on particle agglomeration, with these simulations using the full DVLO theory terms outlined earlier. For these simulations, a base case with a shear Reynolds number of $Re_\tau = 360$ was utilised together with a restitution coefficient e_n = 0.4 and Hamaker constant H =22.3 zJ, representative of 100 μm diameter calcite particles in water (shear Stokes number St^+=1.95), a commonly used simulant for nuclear waste material in slurry flows. To account for the influence of the EDL, the key parameters incorporated were the reduced surface potential $\Theta = 20\text{mV}$, inverse Debye length κ = 3.04 x 10^{-9} m and the temperature of the suspension $T_f = 293\text{K}$, again chosen to match calcite particles in water. Additionally, it is important to determine whether modifications to EDL-related parameters cause the term to produce a more pronounced effect. All the simulation parameters used within this study are presented in Table 1, where e_n is the collision coefficient of restitution, H is the Hamaker constant and Re_τ is the shear Reynolds number.

Table 1: Simulation mechanical and chemical properties.

Simulation	e_n	H (zJ)	δ_0 (m)	σ (Pa)	Re_τ	κ(m)	T_f (K)	Θ (mV)
I	0.4	22.3	2×10^{-10}	3×10^{8}	360	3×10^{-9}	293	20
II	0.2	22.3	2×10^{-10}	3×10^{8}	360	3×10^{-9}	293	20
III	0.6	22.3	2×10^{-10}	3×10^{8}	360	3×10^{-9}	293	20
IV	0.4	7.84	2×10^{-10}	3×10^{8}	360	3×10^{-9}	293	20
V	0.4	36.8	2×10^{-10}	3×10^{8}	360	3×10^{-9}	293	20
VI	0.4	22.3	2×10^{-10}	3×10^{8}	180	3×10^{-9}	293	20
VII	0.4	22.3	2×10^{-10}	3×10^{8}	360	3×10^{-8}	293	20
VIII	0.4	22.3	2×10^{-10}	3×10^{8}	360	3×10^{-10}	293	20
IX	0.4	22.3	2×10^{-10}	3×10^{8}	360	3×10^{-9}	264	20
X	0.4	22.3	2×10^{-10}	3×10^{8}	360	3×10^{-9}	322	20
XI	0.4	22.3	2×10^{-10}	3×10^{8}	360	3×10^{-9}	293	16
XII	0.4	22.3	2×10^{-10}	3×10^{8}	360	3×10^{-9}	293	24

Figure 4(a) shows predictions of the time evolution of agglomerates of various sizes, from singlets to quintuplets, for the base case with and without the electric double layer term accounted for. Clearly, these results show that there is no significant difference in the rate of agglomerate formation when the electric double layer model is included. The singlet and doublet particles in particular are not significantly affected by the electric double layer effect, with triplets and above showing minimal differences (given the logarithmic ordinate scale).

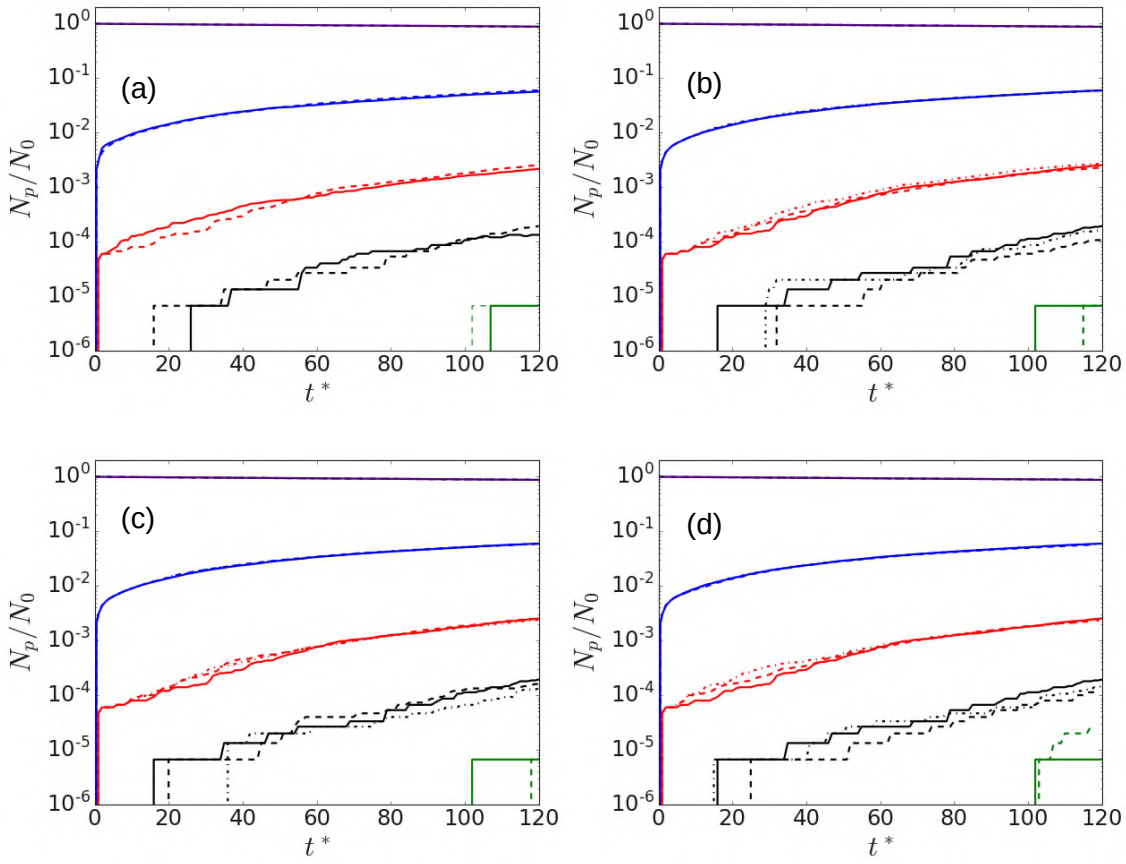

Figure 4: (a) Influence of electric double layer on particle agglomeration, and impact of variations in (b) temperature, (c) reduced surface potential, and (d) inverse Debye length on total number of agglomerates of size N_p normalised by total number of particles as function of time (Indigo – singlets, blue – doublets, red – triplets, black – quadruplets, green – quintuplets; — with EDL, – – without EDL in (a); — T_f = 293K, – – T_f = 322K, –·– T_f = 264K; — Θ = 20 mV, – – Θ = 24 mV, –·– Θ = 16 mV; — κ =3.04×10^{-9} m, – – κ =3.04×10^{-8} m, –·– κ =3.04×10^{-10} m).

It is also important to determine whether modifications to EDL-related parameters cause the term to have a significant influence on particle agglomeration. Temperature plays a critical role in the calculation of the electric double layer repulsion potential. Here, we explore the effect of temperature on agglomeration rate, and the outcomes are then compared to the base case noted above, with the effects of a 10% temperature increase (T_f = 322K) and decrease (T_f = 264K) studied. Figure 4(b) shows the influence of temperature on the total number of agglomerates of

size N_p as a function of t^*, with single particles and agglomerates up to quintuplets again monitored as they change over time. Examining the formation of triplets and quadruplets, it can be seen that lower temperatures encourage particle collisions and the possibility of agglomeration, although this impact is negligible, and temperature change exhibits little impact on the dynamics of the particle interactions. Mortimer and Fairweather (2021) also found that there is relatively little effect of temperature on particle interaction dynamics for micron-scale particles when particle-resolved simulations were performed.

The reduced surface potential is another important parameter in the electric double layer repulsion force and refers to the electrical potential differential between a particle's surface and its surroundings. This can be influenced by a variety of factors that impact the charge distribution and interactions at the particle's surface. A higher temperature can also promote charge mobility and diffusion, which reduces surface potential and redistributes charge. The reduced surface potential is also a result of the interaction of various elements, including the zeta potential, the elementary electric charge, and the ionic valency of the electrolyte. The effect of modifying the potential on the number of agglomerates is considered in Figure 4(c). Again, for the base case with EDL forces accounted for, with Θ=20 mV, and a higher reduced surface potential, the production of agglomerates with constituent numbers ranging from doublets to quintuplets is observed, whereas only triplets are generated for a lower reduced surface potential. For all three reduced surface potential simulations, however, the formation of doublet particles or the tendency of singlets to form larger agglomerates stays roughly the same with time. Generally, modifications to the reduced surface potential again lead to negligible effects on the agglomeration rate for calcite particles in water.

Lastly, the effect of the inverse Debye length, also referred to as the Debye screening length, κ, on agglomeration rate was examined. This modification, which results from the interaction of charged particles in the electrolyte solution and a particle, is a measure of the thickness of the electric double layer surrounding the particle and is another important parameter in DLVO theory. The Debye screening length is dependent on the ionic strength of the aqueous phase, which can be modified through the addition of salts. The production of doublet, triplet and quadruplet agglomerates in Figure 4(d) once again demonstrates that variations in the inverse Debye length have relatively little effect on the rate of agglomeration, even across a three orders of magnitude change.

All these findings justify use of the energy-based particle agglomeration model which neglects the effects of electric double layer repulsion on particle agglomeration.

3.3 Influence of normal restitution coefficient

The influence of changes in the coefficient of restitution, an important parameter which can be modified through a variety of means such as through particle coating or by adjusting the temperature of the system, is considered first. Figure 5(a) illustrates the time evolution of the number of agglomerates of increasing size ranging from singlets to sextuplets, and shows the influence of the restitution coefficient on agglomeration dynamics. Agglomeration begins to occur at t^* = 0.01, and for the base case value of the restitution coefficient employed, e_n = 0.4, the primary particle number has fallen from 150k originally injected to ~132k particles, or by around 12%, by t^* = 120. To investigate the effect of modifying the restitution coefficient on collision and agglomeration while keeping all other simulation parameters for calcite at their default values, two further simulations with e_n = 0.2 and 0.6 were performed at the same flow Reynolds number. The singlet particles reduced from 150k particles to ~118k particles (by ~21.3%) and ~141k particles (by ~6.1%) for restitution coefficients of e_n= 0.2 and e_n= 0.6, respectively. The rate of agglomeration therefore increases, and the time required for the formation of higher-order aggregates decreases, as the restitution number decreases. When results for the e_n= 0.2 and e_n= 0.6 simulations are compared to those with a restitution coefficient e_n= 0.4, an additional ~9.3% of singlet particles aggregate for e_n= 0.2 whereas ~5.9% fewer agglomerate for e_n= 0.6.

The increase in the rate of formation of larger agglomerates with decreasing restitution coefficient is due to more energy being dissipated in a collision leading to increased chances for the agglomeration condition to be satisfied. As the simulations progress, the existence of larger particles also means that the agglomeration likelihood diminishes due to larger colliding particles possessing lower van der Waals attraction and more total collision energy. Interestingly, given that the same initial low Stokes number particle was used in all simulations, differing agglomerate sizes are clearly formed at different rates for the three values of restitution coefficient considered.

Figure 5 also displays the influence of the normal restitution coefficient on the total number of cumulative particle-particle collisions, N_{col}, the total number of the cumulative particle-particle agglomerations, N_{agg}, and the temporal evolution of the agglomeration efficiency, N_{agg}/N_{col}. For restitution coefficients e_n= 0.2, 0.4 and 0.6, approximately 2.5 million, 2 million and 1.5

million individual particle-particle collisions are observed, resulting in nearly 1.9 million, ~9,500 and ~5,000 pairs of particles aggregating, respectively, over the course of the simulations. The normal restitution coefficient is thus shown to demonstrate a significant impact on particle collisions and agglomeration such that the lower the restitution coefficient, the more frequently particles collide and aggregate. The temporal evolution of the ratio of inter-particle collisions which lead to an agglomeration event to the total number of inter-particle collisions (i.e. the agglomeration efficiency) in Figure 5 is underpinned by a trade-off between collision frequency and the dynamics associated with particles in various regions of the flow. For instance, close to the wall, particles collide with increased relative velocities due to the turbulent motion associated with that region, leading to a lower likelihood of agglomeration. In line with previous observations, the lowest coefficient of restitution leads to the greatest chance of aggregation, given a collision has already occurred, with the efficiency remaining steady throughout the simulation time considered in all three cases after an initial period during which the rate increases.

The spatial distribution of collision and agglomeration events is considered in more detail in Figure 6. For a restitution coefficient e_n = 0.2, as the pipe centreline is approached, fewer collisions occur, with the frequency of collisions found to be highest close to the wall. Due to the high inelasticity of particle-particle collisions at low restitution coefficients (Eq. (19)), which causes particles to lose a considerable amount of kinetic energy during a collision resulting in a low relative velocity, particles are more prone to aggregate upon collision. It is also interesting to note that agglomeration events occur almost uniformly across the pipe cross-section, with slightly fewer aggregates forming close to the wall. With an increase in the normal restitution coefficient to e_n = 0.6, the distribution of collision events across the pipe radius shows a significant reduction in number, though the shape of the distribution remains qualitatively similar. Close to the wall, there are a relatively large number of collisions occurring even though the kinetic energy is mainly conserved and the particles keep a sizable amount of their pre-collision velocity at this moderately high restitution coefficient. Due to significantly higher mean relative particle collision velocities, as compared to those for lower restitution coefficients (e_n = 0.2 or 0.4), more recoil-type behaviour and less agglomeration results when two particles collide. Overall, the results of Figure 6 demonstrates that agglomeration events occur relatively consistently across the pipe cross-section at all restitution coefficient values, with collision events decreasing with distance away from the wall in all cases.

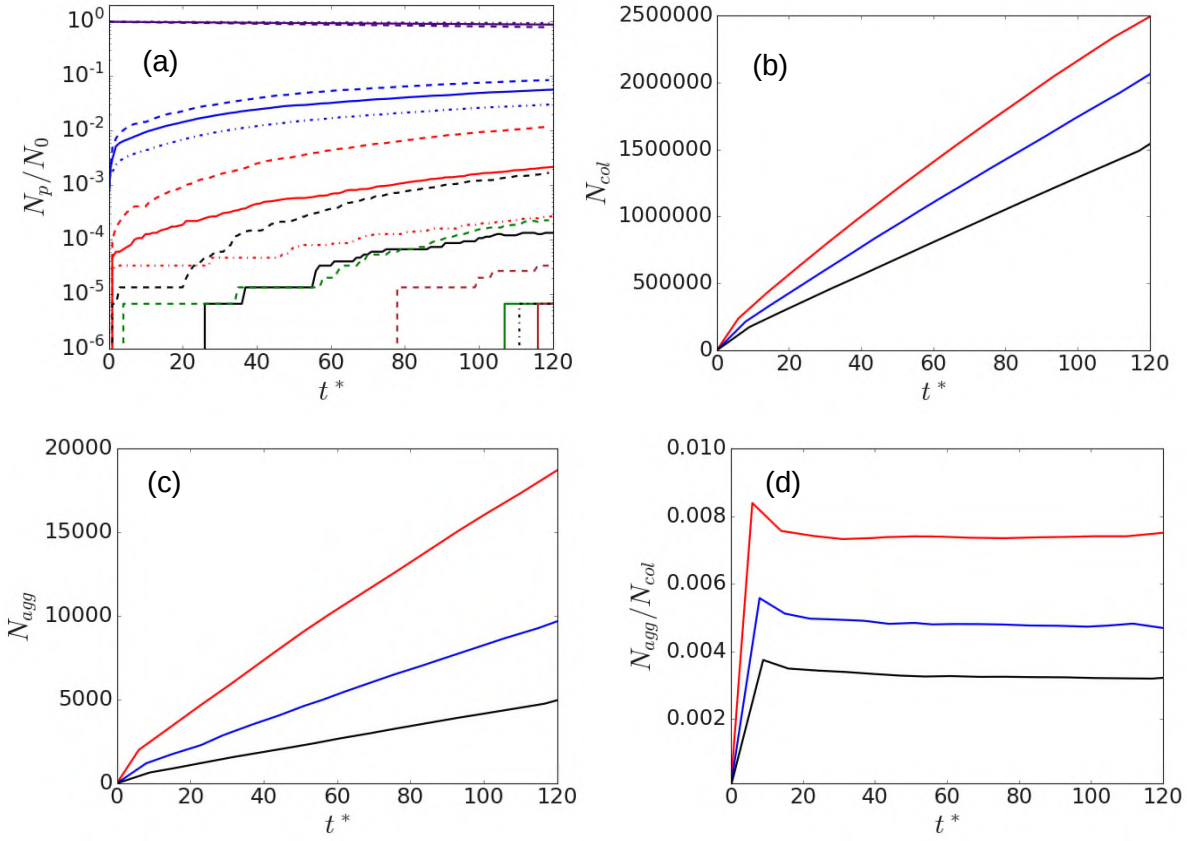

Figure 5: (a) Influence of normal restitution coefficient on total number of agglomerates of size N_p normalised by total number of particles as function of time (Indigo – singlets, blue – doublets, red – triplets, black – quadruplets, green – quintuplets, brown – sextuplets; — e_n= 0.4, – – e_n= 0.2, –·– e_n= 0.6), (b) distribution of total number of particle-particle collisions, N_{col}, and (c) agglomerates, N_{agg}, with time, and (d) temporal evolution of agglomeration efficiency, N_{agg}/N_{col} (red – e_n= 0.2, blue – e_n= 0.4, black – e_n= 0.6).

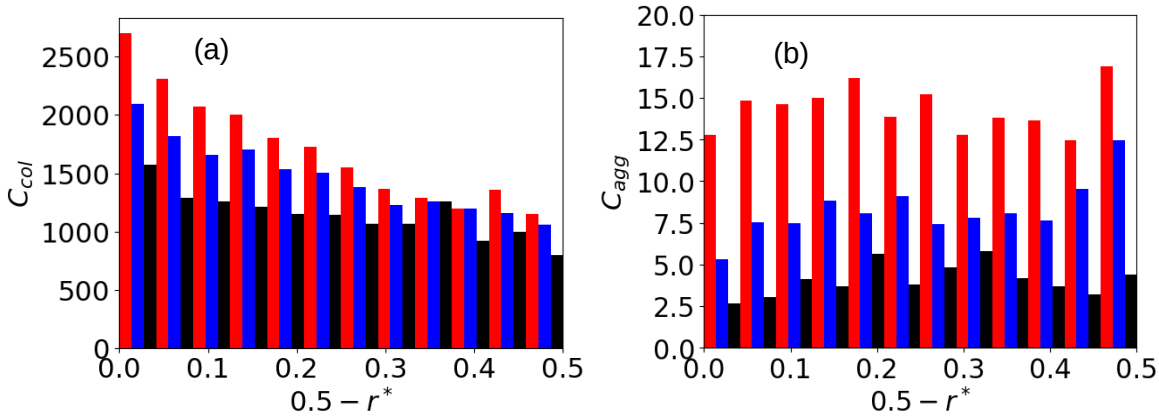

Figure 6: (a) Number of collision and (b) agglomeration events across pipe radius, normalised by volume, sampled at t^* = 70 (red – e_n = 0.2, blue – e_n = 0.4, black – e_n =0.6).

Figure 7 shows the particle dynamic properties for different restitution coefficients in the viscous sublayer ($0 \leq 0.5 - r^* < 0.0135$), buffer layer ($0.0135 \leq 0.5 - r^* < 0.083$), log-law ($0.083 \leq 0.5 - r^* < 0.1$) and bulk flow ($0.1 \leq 0.5 - r^* \leq 0.5$) regions of the pipe at Stokes number St^+=1.95. These probability density functions (PDFs) were examined in order to gain a better understanding of the implications of changes in the restitution coefficient on the local dispersive and inter-particle interaction behaviour, and therefore on collision and agglomeration. PDFs of the streamwise, radial, azimuthal and slip velocities are shown for the various restitution coefficient in the four flow regions. Particle dynamics in the viscous sublayer and bulk regions of the flow are seen to be considerably influenced by changes in the restitution coefficient, as evidenced by the PDFs of the particle streamwise and radial velocities, although the effect of any change is minimal in the azimuthal direction. PDFs of the slip velocity are also given in Figure 7, and these tend to increase with a decrease in the restitution coefficient, as would be expected for more inertial particles. The restitution coefficient is therefore shown to have a significant impact on the resulting particle behaviour, which then further impacts the dynamics of collision and agglomeration, particularly in the viscous sublayer and bulk regions of the flow.

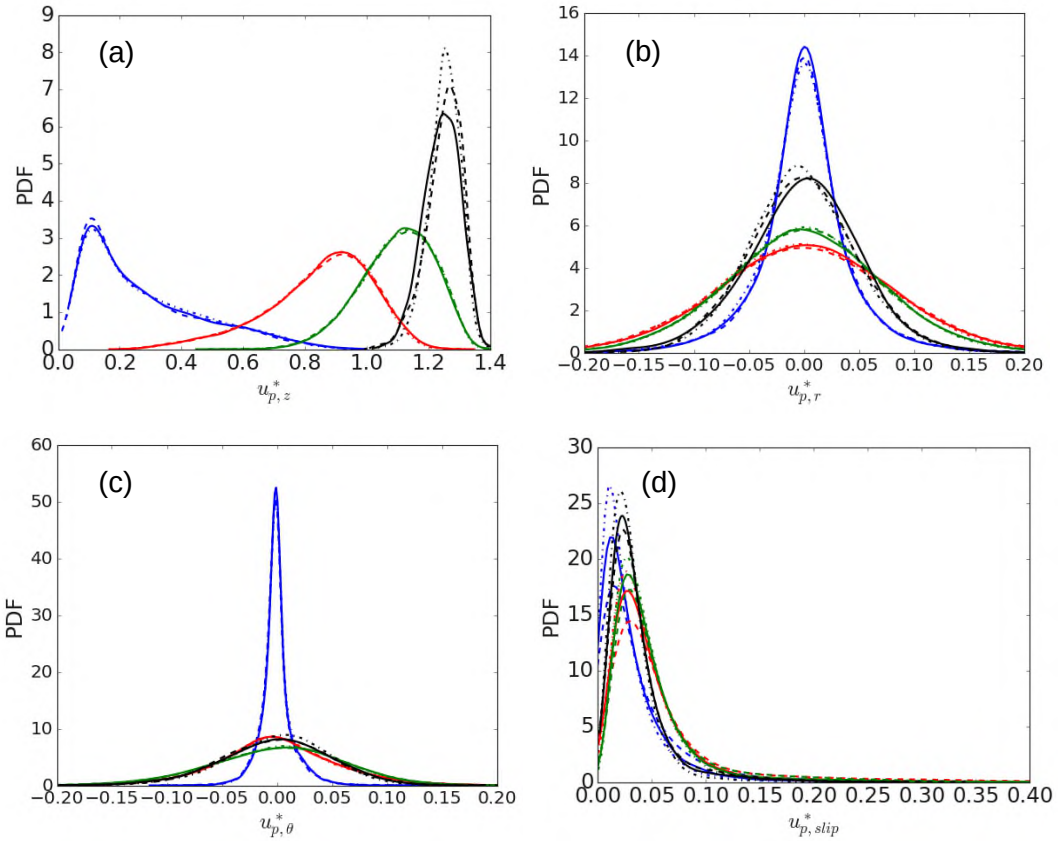

Figure 7: Probability density functions of (a) streamwise velocity, (b) radial velocity, (c) azimuthal velocity, and (d) slip velocity for varying restitution coefficient in viscous sublayer, buffer layer, log-law and bulk flow regions (blue – viscous sublayer, red – buffer layer, green – log-law region, black – bulk flow region; — e_n= 0.4, – – e_n= 0.2, –·– e_n= 0.6).

3.4 Influence of Hamaker constant

The Hamaker constant, a chemical parameter which influences the strength of particle-particle van der Waals interactions, is an important quantity to investigate when examining the collision and agglomeration of micron-scale particles. It can be determined empirically as well as theoretically. For example, according to the macroscopic theory of Lifshitz (1956), it can be computed theoretically by studying the frequency dependence of the dielectric function. Van der Waals forces are only effective over very short ranges, with the dispersion potential degrading more quickly in what is known as the retarded regime when the particle interactions are too distant from one another. Here, we again study variations in the Hamaker constant which can be implemented practically by the addition of salt or modifying the temperature of the system.

It has been demonstrated in previous studies (Mortimer and Fairweather, 2021) that the Hamaker constant has a significant impact on the mean collision velocity of interacting particles which necessarily affects agglomeraiton. Figure 8 demonstrates the effect of Hamaker constant on the total number of agglomerates of size N_p as a function of t^*. The generation of agglomerates with particle numbers ranging from singlets to sextuplets is observed for the highest Hamaker constant, whereas only up to quadruplet agglomerates is observed for the lowest Hamaker constant value, such that increases in H lead to increasing agglomerate sizes. After t^* = 1, the Hamaker constant's impact becomes apparent. By the time the simulation reaches t^* = 120, the primary particle number has decreased from 150,000 to 132,011 particles, or approximately 12.0%, for a Hamaker constant value, H = 22.3 zJ. In contrast, for Hamaker constants H=36.76 zJ and H=7.87 zJ, the primary particles were reduced to 118,511 particles (~21.0%) and 141,535 particles (~5.6%), respectively. In comparison to the Hamaker constant H= 22.3 zJ predictions therefore, approximately 8% more primary particles agglomerate for H = 36.76 zJ, while only slightly more than 6% did not for H = 7.84 zJ. The formation of doublets, triplets and larger agglomerates increases with time, and at the end of the simulation the total number of agglomerates observed is 2.79% (doublets), 0.022% (triplets) and 0.00067% (quadruplets) of the total primary particles for the lowest Hamaker constant, H = 7.84 zJ. Similarly, for H = 22.3 zJ, there are approximately 5.64% (for doublets), 0.216% (for triplets), 0.013% (for quadruplets) and 0.00067% (for quintuplets and sextuplets) total agglomerates. The value of H = 36.76 zJ produced the highest agglomeration rate, which was found to be 8.88% (for doublets), 0.945% (for triplets), 0.0876% (for quadruplets) and 0.000867% (for quintuplets and sextuplets).

Figure 8 also illustrates the influence of the Hamaker constant on the total number of cumulative particle-particle collisions, N_{col}, the total number of the cumulative particle-particle agglomerations, N_{agg}, and the temporal evolution of the agglomeration efficiency, N_{agg}/N_{col}. For the largest Hamaker constant, more than 2 million distinct particle collisions occur, with more than 16,000 of them to aggregating. In general, and after an initial period, the total number of particle collisions and agglomerations varies almost linearly with time with a significant dependency on the Hamaker constant. Higher collision frequency and higher agglomeration rates are produced by larger Hamaker constants, with the agglomeration efficiency qualitatively similar to that observed in Figure 5 for the impact of restitution coefficient on agglomeration.

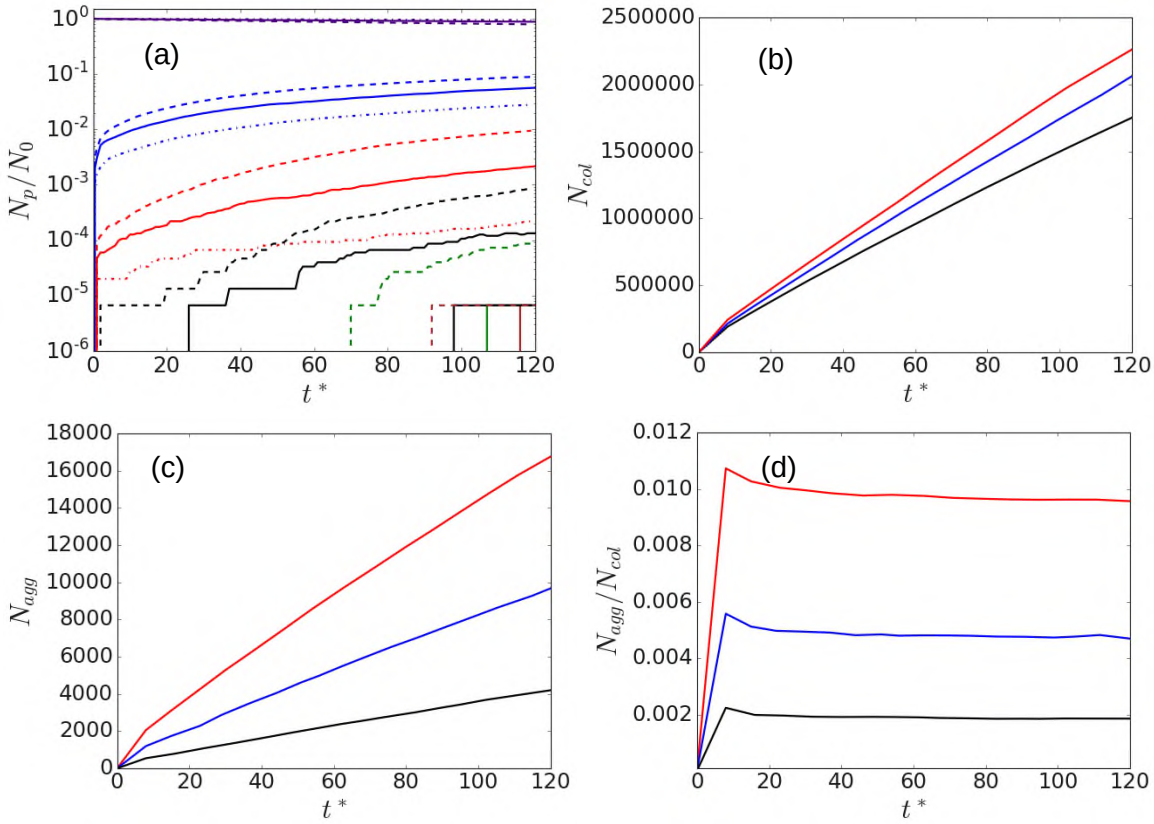

Figure 8: (a) Influence of Hamaker constant on total number of agglomerates of size N_p normalised by total number of particles as function of time (Indigo – singlets, blue – doublets, red – triplets, black – quadruplets, green – quintuplets, brown – sextuplets; — H = 22.3zJ, $--$ $H = 7.84zJ$, $-\cdot-$ $H = 36.76zJ$), (b) distribution of total number of particle-particle collisions, N_{col}, and (c) agglomerates, N_{agg}, with time, and (d) temporal evolution of agglomeration efficiency, N_{agg}/N_{col} (red – $H = 36.76zJ$, blue – $H = 22.3zJ$, black – $H = 7.84zJ$).

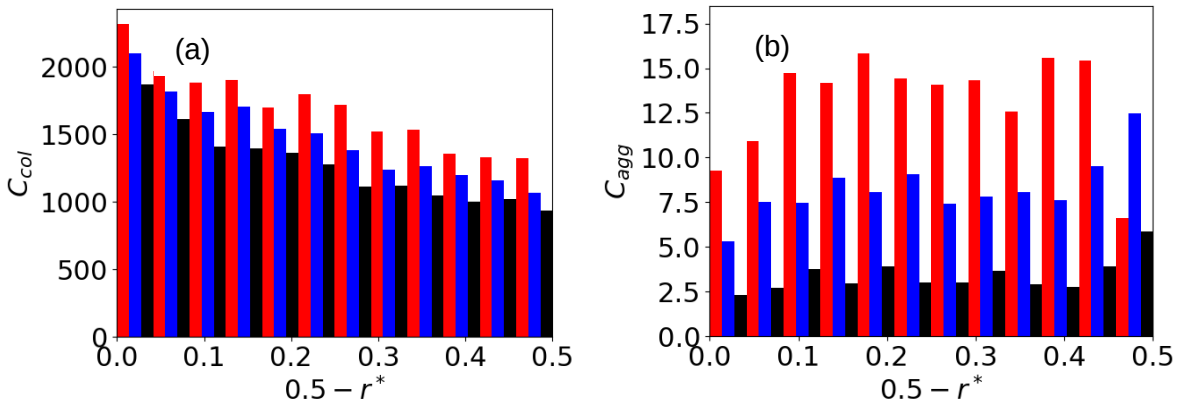

Figure 9: (a) Number of collision and (b) agglomeration events across pipe radius, normalised by volume, sampled at t^*= 70 (red – $H = 36.76zJ$, blue – $H = 22.3zJ$, black – $H = 7.84zJ$).

Figure 9 shows the distribution of collisions and agglomerations across the pipe radius at t^* = 70 for all Hamaker constant values. In all cases, and as in Figure 6, the largest number of collisions occur close to the wall and decrease as the central region of the pipe is approached. Once away from the wall region, agglomeration events again tend to be relatively uniform throughout the rest of the flow. Given that a larger Hamaker constant corresponds to stronger van der Waals interactions, the number of agglomeration events increases with increasing *H*, although close to the wall, where mean relative particle collision velocities are high (with e_n = 0.4), fewer agglomerations occur relative to other regions within the flow. It is also noteble that although there is a relatively large number of particle collisions near the wall for the lowest Hamaker constant, there is significantly less agglomeration of primary particles observed as a result of the weak van der Waals force.

Figure 10 illustrates the influence of Hamaker constant on PDFs of various dynamic properties in the viscous sublayer, buffer, log-law and bulk flow regions of the pipe at Stokes number St^+=1.951. These statistical distributions were again examined to gain insight into the dynamics of particle-particle contacts, as well as impact that the Hamaker constant has on the likelihood that interactions lead to collisions and agglomerations. Dynamics within the viscous sublayer and bulk regions of the flow are again seen to be noticeably influenced by the Hamaker constant, as evidenced by the PDFs of the particle streamwise and radial velocities, although the effect of any change is small in the azimuthal direction. The effect of Hamaker constant changes in the buffer and log-law regions of the flow are generally small, whilst the slip velocity increases

with a decrease in the Hamaker constant. The Hamaker constant therefore has a significant impact on particle behaviour which impacts the dynamics of collision and agglomeration, but this is mainly restricted to the viscous sublayer and bulk regions of the flow.

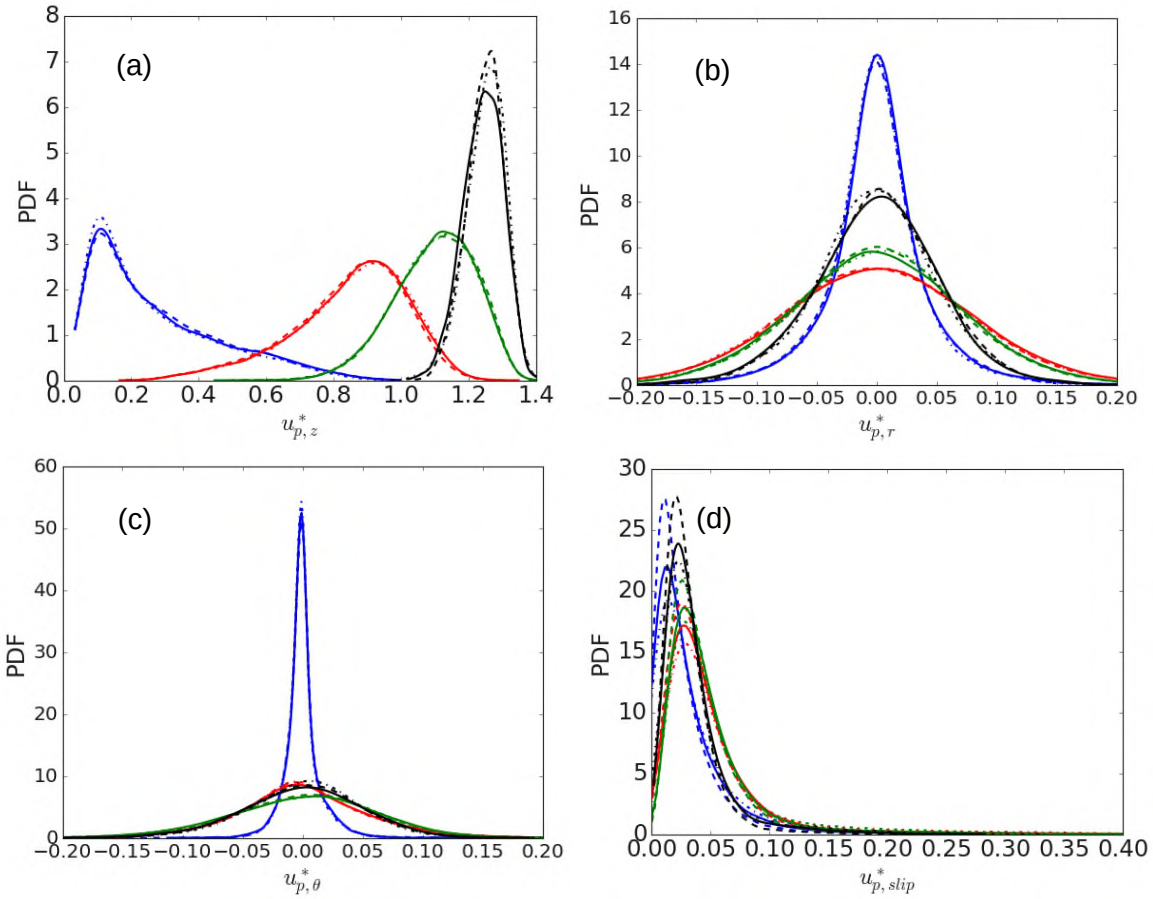

Figure 10: Probability density functions of (a) streamwise velocity, (b) radial velocity, (c) azimuthal velocity, and (d) slip velocity for varying restitution coefficient in viscous sublayer, buffer layer, log-law and bulk flow regions (blue – viscous sublayer, red – buffer layer, green – log-law region, black – bulk flow region; — $H = 22.3zJ$, – – $H = 7.84zJ$, –·– $H = 36.76zJ$).

3.5 Influence of Reynolds number

Finally, to determine how the flow Reynolds number affects particle behaviour, the flow's pressure gradient was reduced on order to achieve a $Re_\tau = 180$ flow, performed using the same computational mesh. It is important to note that in these simulations, the particle properties—specifically, particle diameter and density—were held constant when varying the flow Reynolds number. As a result, the particle Stokes number changes with Reynolds number, reflecting the

practical reality in many industrial systems (e.g., nuclear waste slurry transport) where particle properties are typically fixed, and adjustments to flow conditions are the primary means of process control. Figure 11 illustrates the impact of changes in the Reynolds number on the evolution of the number of agglomerates. Again, the formation of agglomerates with constituent numbers ranging from singlets to sextuplets was found for $Re_\tau = 360$, whereas only quadruplets were seen for the lower Reynolds number. It is also observed that there is an increased collision and agglomeration rate for the higher Reynolds number. This is likely due to the fact that the turbulent region is thinner at increased Reynolds numbers, and since most agglomeration takes place in the bulk flow region, there is a greater chance of particles encountering each other with similar velocities, increasing the chances of agglomeration. At Reynolds number Re_τ = 360, almost 2 million individual particles interact with one another, resulting in the formation of aggregates of approximately 9,672 particles, while at Reynolds number Re_τ = 180, over 1.8 million particle-particle collisions and 6,651 agglomeration events are observed. Overall, the number of particle collisions and agglomerations typically varies approximately linearly with time, with the rate of agglomeration in particular dependent on the Reynolds number. Collision efficiencies are again qualitatively similar to those observed in Figures 5 and 8 for the impact of restitution coefficient and Hamaker constant on agglomeration.

Figure 12 shows the impact of modifying the Reynolds number on the concentration of collision and agglomeration events across the pipe radius sampled at t^* = 70. The trends in collision and agglomeration events are similar to observed previously, with collisions decreasing with distance from the wall, and agglomerations approximately constant throughout the flow outside the wall region. However, at Re_τ=180, the collision rate close to the wall is particularly high, due to lower mean velocities and turbulence levels in this region, although the number of collisions was found to decrease significantly at larger t^*. Similarly, at the higher Reynolds number, the number of agglomerations close to the pipe centre is again larger than elsewhere in the flow, confirming the previous contention that the thinner turbulent region in this flow leads to most agglomeration taking place in the bulk flow region where there is a greater chance of particles encountering each other with similar velocities.

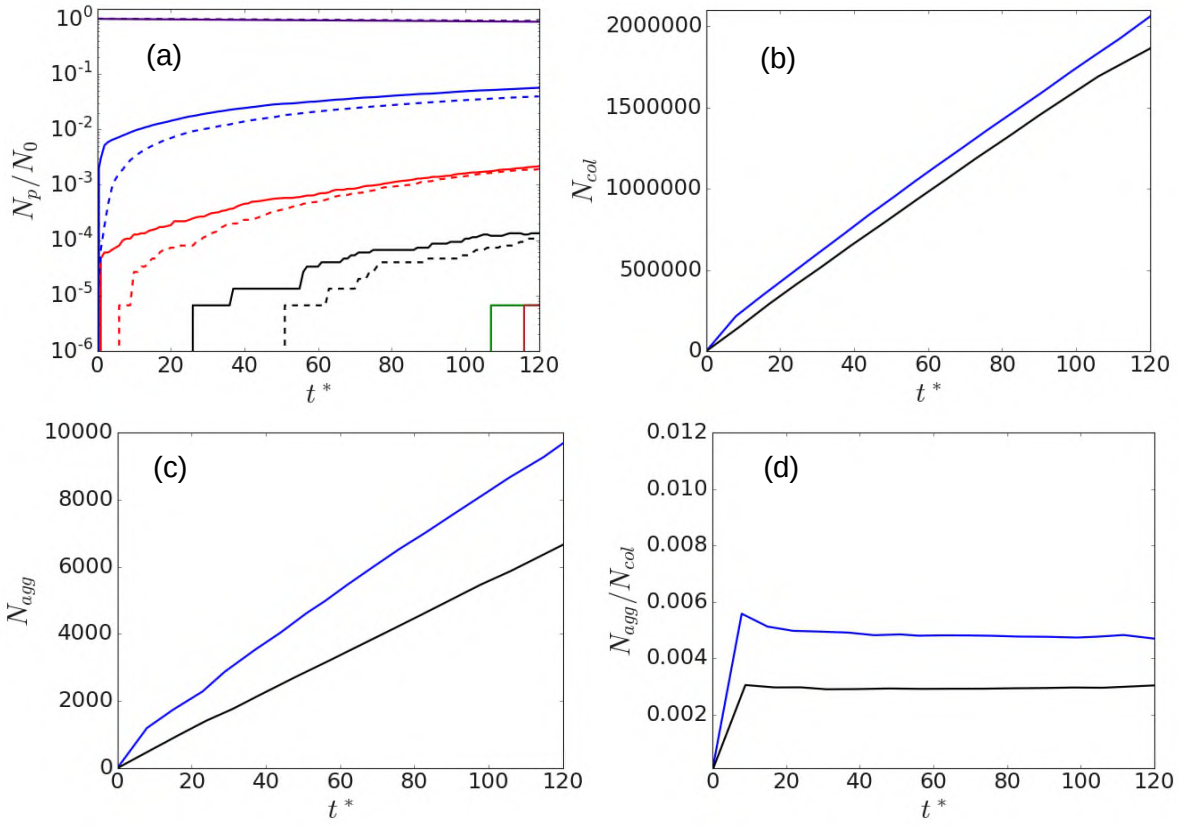

Figure 11: Influence of Reynolds number on total number of agglomerates of size N_p normalised by total number of particles as function of time (Indigo – singlets, blue – doublets, red – triplets, black – quadruplets, green – quintuplets, brown – sextuplets; — Re_τ= 360, – – Re_τ= 180), (b) distribution of total number of particle-particle collisions, N_{col}, and (c) agglomerates, N_{agg}, with time, and (d) temporal evolution of agglomeration efficiency, N_{agg}/N_{col} (blue – Re_τ= 360, black – Re_τ= 180).

Lastly, the influence of Reynolds number on the PDFs of dynamic particle properties in the various regions of the pipe flow is shown in Figure 13. Clearly, the Reynolds number has a significant influence in all regions of the flow. The streamwise velocities in the buffer layer and log-law regions are higher for the increased Reynolds number, though they are reduced in the viscous sublayer and bulk flow regions. In all cases the azimuthal and radial velocity component distributions widen with increased Reynolds number, with a broader range of velocities sampled. The collapse of azimuthal particle velocity profiles in the viscous sublayer at $Re_\tau = 180$ to the more distributed profiles at $Re_\tau = 360$ can be attributed to the diminished turbulent intensity and

weakened secondary flow structures at the lower Reynolds number. At higher Reynolds numbers, coherent structures such as streamwise vortices and low-speed streaks promote azimuthal velocity fluctuations, which in turn drive more significant dispersion of particles in the azimuthal direction. In contrast, the reduced turbulence levels and less energetic near-wall structures at $Re_\tau = 180$ lead to lower spanwise shear forces, suppressing azimuthal dispersion and resulting in a collapse of particle velocities in this region, leading to a narrower distribution. The slip velocities also tend to increase, meaning that the particles are decorrelated more significantly from the local fluid velocity when the Reynolds number is increased.

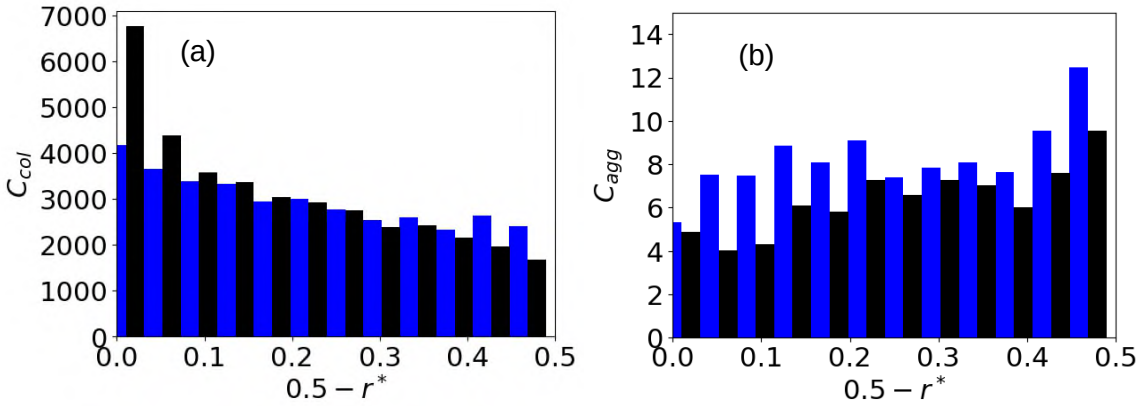

Figure 12: (a) Number of collision and (b) agglomeration events across pipe radius, normalised by volume, sampled at t^* = 70 (blue – Re_τ = 360, black – Re_τ= 180).

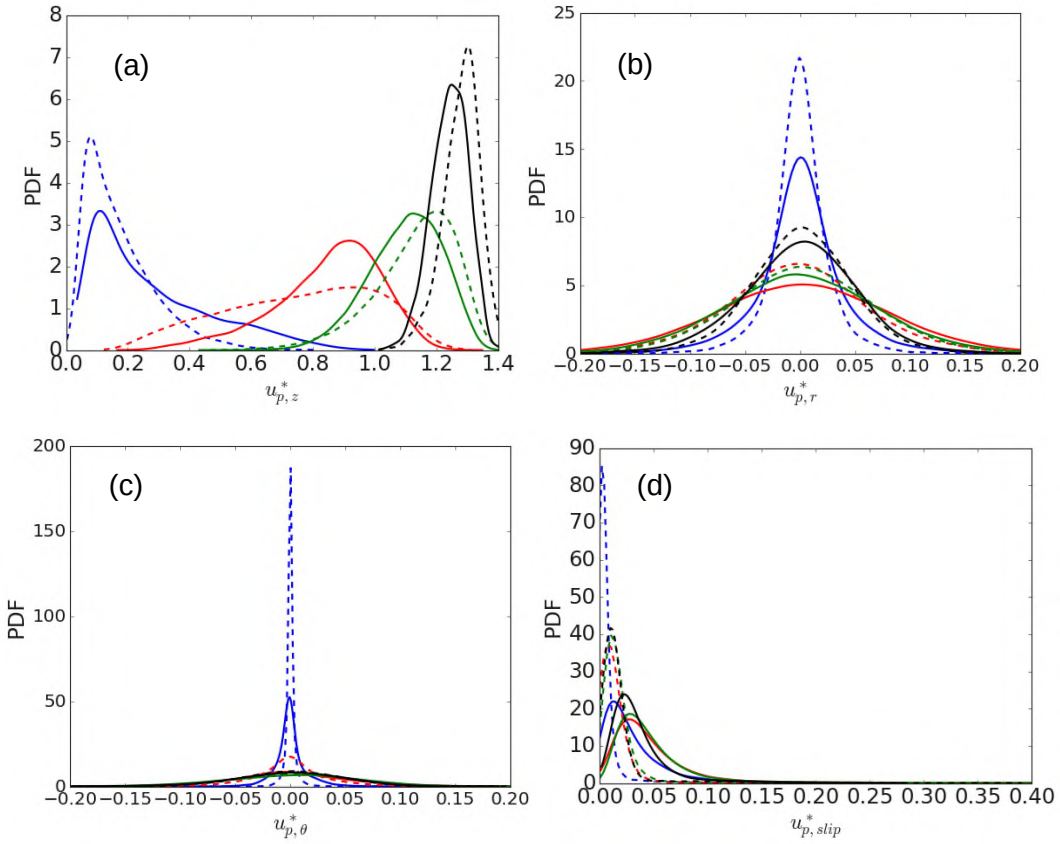

Figure 13: Probability density functions of (a) streamwise velocity, (b) radial velocity, (c) azimuthal velocity, and (d) slip velocity for varying restitution coefficient in viscous sublayer, buffer layer, log-law and bulk flow regions (blue – viscous sublayer, red – buffer layer, green – log-law region, black – bulk flow region; – – Re_τ= 180, — Re_τ= 360).

3.6 Collision dynamics and summary

Figure 14 shows the mean relative particle collision velocity for the various restitution coefficient, Hamaker constant and Reynolds number values considered previously. This velocity is a key parameter in collision dynamics since it determines the kinetic energy of any collision. Values of this relative collision velocity are significantly higher towards the wall and decrease exponentially towards the pipe centre, indicating that agglomeration is more likely within the core regions of the pipe, in agreement with earlier observations. Modifications to key chemical and physical parameters demonstrate that particle collision dynamics change throughout the flow. Lowering the restitution coefficient decreases the collision velocity close to the wall, likely due to larger

aggregates formed in the bulk flow region of the pipe, which migrate to the wall region through turbophoresis (since their Stokes number increases), where they encounter other particles with uncorrelated velocities. Similarly, lowering the Hamaker constant leads to a reduction in the collision velocity, though only slightly. By reducing the amount of agglomeration through a reduction of the Hamaker constant, the amount of particles with increased Stokes numbers will also be reduced leading to more particles with velocities correlated with those of the local flow field and so collision velocities will be lowered. By increasing the Hamaker constant, more collisions at low kinetic energies will result in agglomeration, taking place mostly in the core region of the pipe. These agglomerates may then remain in that region, still reasonably well correlated with the flow velocity and the velocities of nearby particles, meaning collision velocities will be lower. Differences caused by changes in Reynolds number are small in comparison to those effected by restitution coefficient and Hamaker constant variation.

In Figure 15 mean particle concentration profiles are also illustrated across the pipe at $t^* = 70$, with the values given normalised by the initially injected concentration, C_0. The concentration is seen to be largely unaffected by restitution coefficient and Hamaker constant changes, however, slightly higher concentration variation is observed with changes in Reynolds number.

Lastly, the influence each parameter studied has on the particle-laden flow dynamics and agglomeration behaviour is compared and summarised in Figure 16. This figure illustrates how the normal restitution coefficient, Hamaker constant and Reynolds number affect the agglomeration efficiency as the simulation progresses. The most evident finding from the figure is that large Hamaker constant values increase the agglomeration rate, followed by a similar impact through reductions in the coefficient of restitution. According to these results, it can be concluded that the restitution coefficient, Hamaker constant and Reynolds number all have a significant impact on the agglomeration efficiency, with increasing Hamaker and reducing the coefficient of restitution having strongest influence.

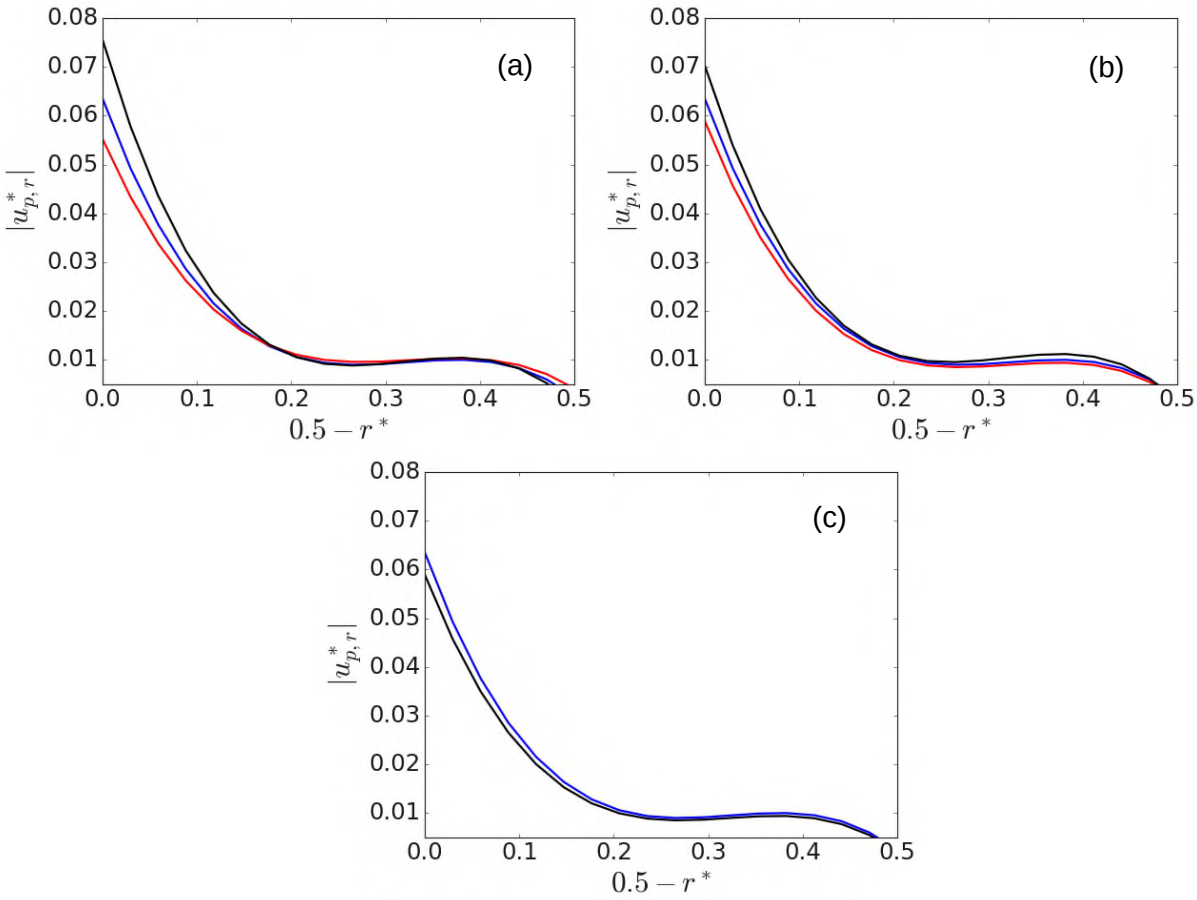

Figure 14: Variation of mean relative particle collision velocity sampled at t^* = 70 across the pipe with (a) restitution coefficient (black – e_n= 0.6, blue – e_n= 0.4, red – e_n= 0.2, with $H = 22.3zJ$, Re_τ= 360), (b) Hamaker constant (black – $H = 36.76zJ$, blue – $H = 22.3zJ$, red – $H = 7.84zJ$, with e_n= 0.4, Re_τ= 360) and (c) Reynolds number (blue – Re_τ= 360, black – Re_τ= 180, with e_n= 0.4, $H = 22.3zJ$).

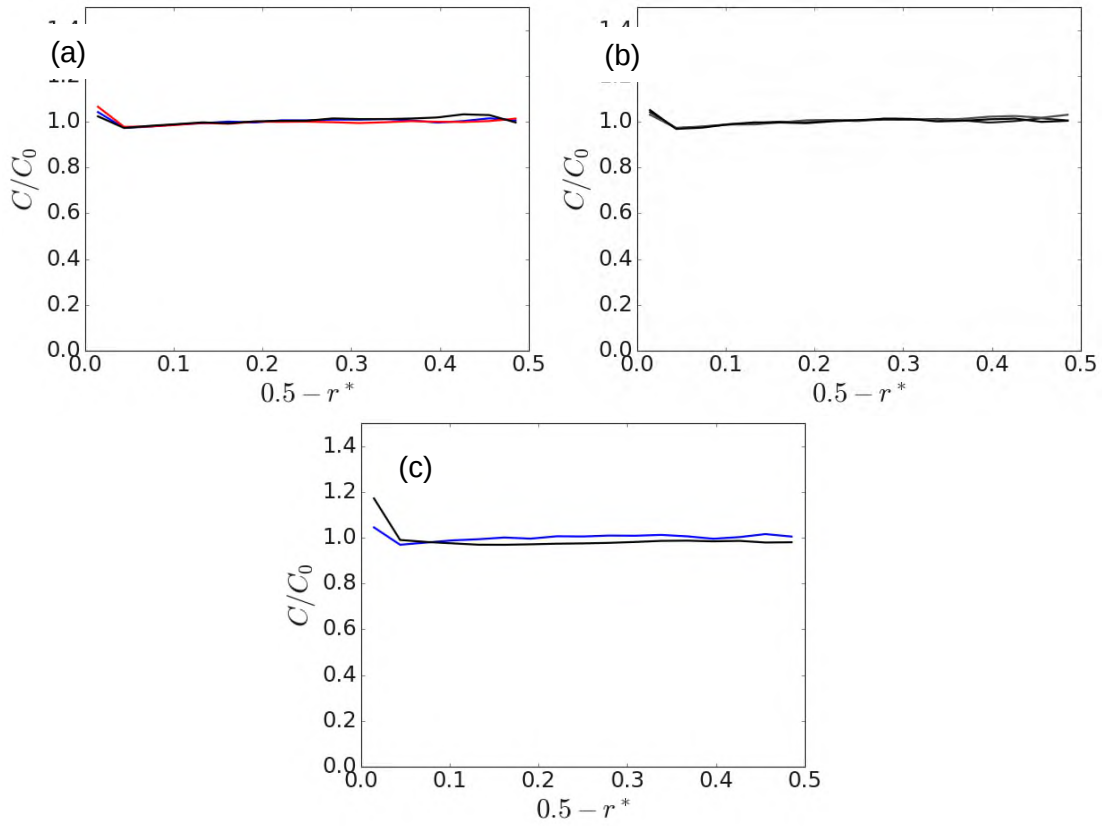

Figure 15: Variation of particle concentration sampled at t^* = 70 across the pipe with (a) restitution coefficient (black – e_n= 0.6, blue – e_n= 0.4, red – e_n= 0.2, with $H = 22.3zJ$, Re_τ= 360), (b) Hamaker constant (blue – $H = 36.76zJ$, black – $H = 22.3zJ$, red – $H = 7.84zJ$, with e_n= 0.4, Re_τ=360) and (c) Reynolds number (blue – Re_τ= 360, black – Re_τ= 180, with e_n= 0.4, $H = 22.3zJ$).

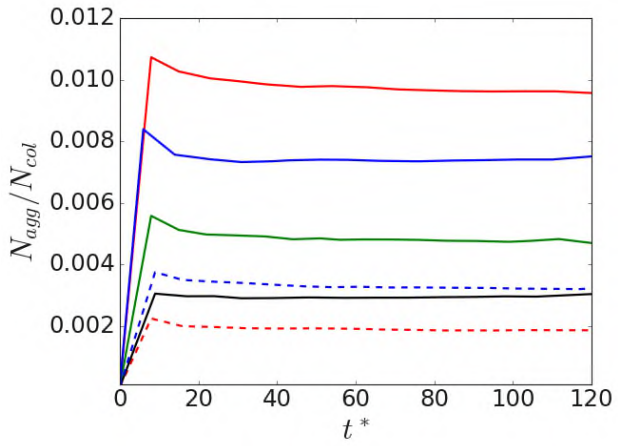

Figure 16: Variation of temporal evolution of agglomeration efficiency, N_{agg}/N_{col}, with restitution coefficient, Hamaker constant and Reynolds number (red solid – e_n= 0.4, H = 36.76zJ, Re_τ = 360; blue solid – e_n= 0.2, H = 22.3zJ, Re_τ = 360; green solid – e_n= 0.4, H = 22.3zJ, Re_τ = 360; blue dashed – e_n= 0.6, H = 22.3zJ, Re_τ = 360; black solid – e_n= 0.4, H = 22.3zJ, Re_τ =180; red dashed – e_n= 0.4 H = 7.84zJ, Re_τ =360).

4. CONCLUSIONS AND OUTLOOK

This study has considered the effect of behavioural modification techniques within wall bounded particle-laden turbulent pipe flows which can be used to influence particle dispersion, agglomeration and ultimately particle deposition. Initially, multi-phase flow simulations were validated against previous studies with good agreement obtained. To establish the influence of behavioural modification techniques, a range of turbulent pipe flows with different particle electrochemical and fluid properties were then simulated. The use of modifications to the fluid and solid particle properties to promote desired outcomes such as reducing particle agglomeration have been considered. This has entailed the implementation of four-way coupling between the particles and the fluid flow, as well as the incorporation of models for particle interaction and agglomeration.

To predict particle aggregation caused by collision interactions, an energy-balance based agglomeration determination technique was employed. The variation of influential parameters including the reduced surface potential, inverse Debye length, temperature of the suspension, the restitution coefficient, Hamaker constant and Reynolds number were all studied to determine the

impact of the modifications. These modifications alter particle interactions by influencing various terms in the Derjaguin-Landau Verwey-Overbeek (full DLVO) theory interaction potentials.

From the work reported, it can be concluded that the electric double layer has an insignificant effect on collision and agglomeration rate. One of the more significant findings to emerge from this study is that the size and rate at which agglomerates are formed has an inverse relationship to the restitution coefficient. Furthermore, we observe that collisions take place more frequently close to the pipe wall, though this does not appear to have much influence on the agglomeration event distribution, which is relatively homogeneous throughout the pipe.

Similar studies have been performed for Hamaker constant and Reynolds number variation. The evidence from the simulations performed shows that the Hamaker constant and Reynolds number again have a large impact on particle-particle interactions. Both collision and agglomeration rates have a linear dependency on the Hamaker constant and Reynolds number within the pipe. A higher Hamaker constant increases the rate at which agglomeration takes place, whilst increases in Reynolds number also increases the likelihood of collision and agglomeration, despite enhanced turbulence leading to more ballistic collisions.

It is important to acknowledge certain limitations of the present modelling framework. First, while four-way coupling is employed, the two-way fluid-particle momentum exchange considers only the drag force contribution. Other hydrodynamic forces such as lift and added mass are not included in the feedback to the carrier phase, based on previous findings that these terms are typically of smaller magnitude (Mortimer et al., 2019). However, in regions of strong shear or near the wall, these neglected feedback forces may locally influence turbulence modulation and hence particle collision dynamics. Second, as particle agglomeration proceeds, the equivalent diameters of some aggregates can approach or exceed the size of the smallest near-wall grid cells. In these cases, the point-particle assumption becomes less accurate, and near-wall particle-fluid interactions, including lubrication and finite-size effects, are not explicitly resolved. Consequently, predicted collision and agglomeration rates in the immediate wall region should be interpreted with this limitation in mind. It should also be noted that the restitution coefficient and Hamaker constant values used in this study are based on ranges reported in the broader colloidal and particulate flow literature, rather than values specifically measured for nuclear waste slurry systems. As such, while the trends observed in this study (e.g., the strong influence of restitution coefficient and Hamaker constant on agglomeration dynamics) are expected to hold qualitatively,

accurate prediction of agglomeration behaviour for nuclear applications would benefit from targeted experimental studies to determine these parameters for representative waste particles in liquid flows. Future work will aim to incorporate full hydrodynamic force coupling and adaptive grid or finite-size corrections to better capture the behaviour of larger aggregates near solid boundaries.

The present study has been one of the first attempts to thoroughly examine the impact of various terms in DLVO theory on collision and agglomeration rates in a practical pipe geometry. Additional research is underway to further investigate the combination of cases that resulted in high collision and agglomeration rates (such as low restitution coefficient, high Hamaker constant and high Reynolds number) and those that resulted in low collision and agglomeration rates (such as high restitution coefficient, low Hamaker constant and low Reynolds number). Work to investigate the way behavioural modification impacts particle deposition and the formation of deposited particle beds within pipes is also ongoing.

5. ACKNOWLEDGEMENTS

The authors are grateful for funding from the UK Engineering and Physical Sciences Research Council and the University of Leeds through the TRANSCEND (Transformative Science and Engineering for Nuclear Decommissioning) project (EP/S01019X/1).

REFERENCES

Boersma, B. J., 2013. Direct numerical simulation of turbulent pipe at high Reynolds numbers, velocity statistics and large scale motions. In Eighth International Symposium on Turbulence and Shear Flow Phenomena. Begel House Inc.

Breuer, M., Alletto, M., Flow, F., 2012. Efficient simulation of particle-laden turbulent flows with high mass loadings using LES. Int. J. Heat Fluid Fl. 35, 2-12.

Breuer, M., Almohammed, N., 2015. Modeling and simulation of particle agglomeration in turbulent flows using a hard-sphere model with deterministic collision detection and enhanced

structure models. Int. J. Multiph. Flow 73, 171-206.

Chan, L., Zahtila, T., Ooi, A. and Philip, J., 2021. Transport of particles in a turbulent rough-wall pipe flow. J. Fluid Mech. 908, A1

Chun, J., Oh, T., Luna, M., Schweiger, M., 2011. Effect of particle size distribution on slurry rheology: Nuclear waste simulant slurries. Colloids Surface A 384, 304-310.

Clift, R., Grace, J.R., Weber, M.E., 2005. Bubbles, Drops, and Particles. Courier Corporation, New York.

Dandy, D. A., Dwyer, H.A., 1990. A sphere in shear flow at finite Reynolds number: Effect of shear on particle lift, drag, and heat transfer. J. Fluid Mech. 216, 381-410.

De-Leon, H., Pederiva, F., 2020. Particle modeling of the spreading of coronavirus disease (COVID-19). Phys. Fluids 32, 087113.

Derjaguin, B., Landau, L., 1941. Theory of the stability of strongly charged lyophobic sols and of the adhesion of strongly charged particles in solutions of electrolytes. Acta Physicochim. URSS 14, 633-662.

Eaton, J. K., Fessler, J., 1994. Preferential concentration of particles by turbulence. Int. J. Multiph. Flow 20, 169-209.

Eggels, J.G.M., Unger, F., Weiss, M.H., Westerweel, J., Adrian, R.J., Friedrich, R., and Nieuwstadt, F.T.M., 1994. Fully developed turbulent pipe flow: a comparison between direct numerical simulation and experiment. J. Fluid Mech. 268, 175-210.

Elghobashi, S., An updated classification map of particle-laden turbulent flows. In: IUTAM Symposium on Computational Approaches to Multiphase Flow (2005).

Elghobashi, S., Truesdell, G.C., 2006. Direct simulation of particle dispersion in a decaying isotropic turbulence. J. Fluid Mech. 242, 655-700.

El Khoury, G.K., Schlatter, P., Noorani, A., Fischer, P.F., Brethouwer, G., Johansson, A.V., 2013. Direct numerical simulation of turbulent pipe flow at moderately high Reynolds numbers. Flow

Turbul. Combust. 91, 475-495.

Fairweather, M., Yao, J., 2009. Mechanisms of particle dispersion in a turbulent, square duct flow. AIChE J. 55, 1667-1679.

Ferrante, A., Elghobashi, S., 2003. On the physical mechanisms of two-way coupling in particle-laden isotropic turbulence. Phys. Fluids 15, 315-329.

Fessler, J.R., Kulick, J.D., Eaton, J.K., 1994. Preferential concentration of heavy particles in a turbulent channel flow. Phys. Fluids 6, 3742-3749.

Fischer, P.F., Lottes, J.W., and Kerkemeier, S.G., Nek5000, http://nek5000.mcs.anl.gov (2008)

Geurts, B.J., Clercx, H.J.H., Uijttewaal, M.A., Eds., 2007. Particle-laden Flow: From Geophysical to Kolmogorov Scales. Springer, Dordrecht.

Henry, C., Minier, J., Pozorski, J., Lefèvre, G., 2013. A new stochastic approach for the simulation of agglomeration between colloidal particles. Langmuir 29, 13694-13707.

Kuerten, J.G.M., 2016. Point-particle DNS and LES of particle-laden turbulent flow – A state-of-the-art review. Flow Turbul. Combust. 97, 689-713.

Kuerten, J.G.M., Vreman, A., 2005. Can turbophoresis be predicted by large-eddy simulation? Phys. Fluids 17, 011701.

Lee, J. and Lee, C., 2015. Modification of particle-laden near-wall turbulence: Effect of Stokes number. Phys. Fluids 27, 023303.

Lifshitz, E.M., 1956. The theory of molecular attractive forces between solids. Sov. Phys. J. 2, 73-83.

Marchioli, C., Soldati, A., 2002. Mechanisms for particle transfer and segregation in a turbulent boundary layer. J. Fluid Mech.. 468, 283-315.

Marchioli, C., Soldati, A., Kuerten, J.G.M., Arcen, B., Taniere, A., Goldensoph, G., Squires, K., Cargnelutti, M., Portela, L., 2008. Statistics of particle dispersion in direct numerical simulations

of wall-bounded turbulence: Results of an international collaborative benchmark test. Int. J. Multiph. Flow 34, 879-893.

Maxey, M.R., Riley, J.J., 1983. Equation of motion for a small rigid sphere in a nonuniform flow. Phys. Fluids 26, 883-889.

Mortimer, L.F., Fairweather, M., 2021. Assessment of behavioral modification techniques through immersed boundary method simulation of binary particle interactions in isotropic turbulence. Phys. Fluids 33, 073307.

Mortimer, L.F., Njobuenwu, D.O., Fairweather, M., 2019. Near-wall interparticle collision dynamics in multi-phase turbulent channel flows. Phys. Fluids 31, 063302.

Mortimer, L.F. and Fairweather, M., 2020. Density ratio effects on the topology of coherent turbulent structures in two-way coupled particle-laden channel flows. Phys. Fluids, 32, 103302.

Mortimer, L.F., Njobuenwu, D.O., Fairweather, M., 2020. Agglomeration dynamics in liquid-solid particle-laden turbulent channel flows using an energy-based deterministic approach. Phys. Fluids 32, 043301.

Njobuenwu, D.O., Fairweather, M., Deterministic modelling of particle agglomeration in turbulent flow. In: Proceedings of Eighth International Symposium on Turbulence, Heat and Mass Transfer (2015).

Njobuenwu, D.O., Fairweather, M., 2017. Simulation of deterministic energy-balance particle agglomeration in turbulent liquid-solid flows. Phys. Fluids 29, 083301.

Johnson, P., Bassenne, M. and Moin, P. 2020. Turbophoresis of small inertial particles: theoretical considerations and application to wall-modelled large-eddy simulations. J. Fluid Mech. 883, A27.

Picano, F., Sardina, G., Casciola, C.M., 2009. Spatial development of particle-laden turbulent pipe flow. Phys. Fluids 2, 093305.

Rani, S.L., Winkler, C.M., Vanka, S.P., 2004. Numerical simulations of turbulence modulation by dense particles in a fully developed pipe flow. Powder Technol. 141, 80-99.

Saffman, P., 1965. The lift on a small sphere in a slow shear flow. J. Fluid Mech. 22, 385-400.

Schiller, L., 1934. Neue quantitative Versuche zur Turbulenzentstehung. Z. Ang. Math. Mech. 14, 36-42.

Schiller, L., Naumann, A., 1935. A drag coefficient correlation. Z. Ver. Dtsch. Ing. 77, 318-320.

Schutte, K.C.J., Portela, L.M., Twerda, A., Henkes, R A.W.M., 2015. Hydrodynamic perspective on asphaltene agglomeration and deposition. Energ. Fuel 29, 2754-2767.

Squires, K.D., Eaton, J.K., 1991. Preferential concentration of particles by turbulence. Phys. Fluids 3, 1169-1178.

Stokes, G.G., 1851. On the effect of the internal friction of fluids on the motion of pendulums. Trans. Cambridge Philos. Soc. 9, 8-106.

Verwey, E.J.W., Overbeek, J.T.G., 1955. Theory of the stability of lyophobic colloids. J. Colloid Sci. 10, 224-225.

Vreman, A.W., 2007. Turbulence characteristics of particle-laden pipe flow. J. Fluid Mech. 584, 235-279.

Vreman, B., Geurts, B.J., Deen, N., Kuipers, J., Kuerten, J.G.M., 2009. Two-and four-way coupled Euler-Lagrangian large-eddy simulation of turbulent particle-laden channel flow. Flow Turbul. Comb. 82, 47-71.

Yang, D., Lv, X.Q., Xiong, Y.L., 2019. A computational fluid dynamics study on the solid mineral particles-laden flow in a novel offshore agitated vessel. Proc. Inst. Mech. Eng. Pt. M J. Eng. Marit. Environ. 233, 622-631.

Yao, J., Fairweather, M., 2010. Inertial particle resuspension in a turbulent, square duct flow. Phys. Fluids. 22, 033303.

Zahtila, T., Chan, L., Ooi, A. and Philip, J., 2023. Particle transport in a turbulent pipe flow: direct numerical simulations, phenomenological modelling and physical mechanisms. J. Fluid Mech. 957, A1.

Zhao, L.H., Andersson, H.I. and Gillissen, J.J.J., 2010. Turbulence modulation and drag reduction by spherical particles. Phys. Fluids 22, 081702.